



Deposited via The University of Leeds.

White Rose Research Online URL for this paper:

<https://eprints.whiterose.ac.uk/id/eprint/208798/>

---

**Article:**

Bradley, D. and Li, J. (2024) Reaction propagation, leading to developing detonation, in a rapid compression machine. *Combustion and Flame*, 262. 113331. ISSN: 0010-2180

<https://doi.org/10.1016/j.combustflame.2024.113331>

---

© 2024 The Combustion Institute. Published by Elsevier Inc. This manuscript version is made available under the CC-BY-NC-ND 4.0 license  
<http://creativecommons.org/licenses/by-nc-nd/4.0/>

**Reuse**

This article is distributed under the terms of the Creative Commons Attribution-NoDerivs (CC BY-ND) licence. This licence allows for redistribution, commercial and non-commercial, as long as it is passed along unchanged and in whole, with credit to the original authors. More information and the full terms of the licence here: <https://creativecommons.org/licenses/>

**Takedown**

If you consider content in White Rose Research Online to be in breach of UK law, please notify us by emailing [eprints@whiterose.ac.uk](mailto:eprints@whiterose.ac.uk) including the URL of the record and the reason for the withdrawal request.

# Reaction Propagation, Leading to Developing Detonation, in a Rapid Compression Machine

Derek Bradley\*, Jinzhou Li

School of Mechanical Engineering, University of Leeds, Leeds LS2 9JT, United Kingdom

\*Corresponding author: [D.Bradley@leeds.ac.uk](mailto:D.Bradley@leeds.ac.uk)

---

## Abstract

Optical imaging and pressure measurements are employed to indicate the nature of the varied changes occurring subsequent to compression in a Rapid Compression Machine, RCM, prior to their ultimate termination, usually in a detonation. A stoichiometric mixture of *i*-octane with variable inert diluents was investigated, enabling different compression temperatures to be attained and the varied nature of the subsequent changes to be studied. This was done with eleven *i*-octane/oxygen stoichiometric mixtures, all with different concentrations. The mixtures included some with an autoignitive Negative Temperature Coefficient, NTC. The mixtures were optically observed after compression to 2.0 MPa and pressures continually recorded until the completion of reaction. The compression temperature,  $T_c$ , was progressively increased by changing the compositions of the inert diluents.

At the lowest compression temperature laminar flame propagation was observed, with some wrinkling of the flame. As the temperature increased, calculation and observation confirmed a transition to autoignitive propagation, with a progressively increasing propagation speed of the predominantly autoignitively propagating front. At  $T_c = 740\text{K}$ , in the NTC regime, the autoignitive speed reached a maximum value of about 323 m/s. The NTC had little direct influence upon the ultimate detonation. Further increases in mixture temperature generated increasingly strong acoustic waves. As the acoustic velocity was approached, whether these changes would culminate in a detonation was dependent upon whether the approaching excitation temperature for the necessary accompanying heat release would be sufficient. Ultimately, it depended on whether the value of  $\zeta = a/u_a$  was low enough, and that of  $\varepsilon = \frac{r_0}{a\tau_e}$  was high enough to reside within the Detonation Peninsula. Ultimately quite strong detonations were obtained, verging on super-knock. As the different changes developed, the pressure records showed fluctuations of increasing amplitude. The normalised pressure fluctuations,  $\Delta P/P$ , were found to increase with a Detonation Parameter,  $\beta = (\varepsilon/\zeta)$ .

*Keywords: Autoignitive propagation; Reaction propagation speed; Optical imaging, RCM; Auto-ignition; Detonation Peninsula; Negative Temperature Coefficient; Detonation Parameter; Super-knock.*

---

## Novelty and Significance

1. An RCM is employed to study the autoignition of a mixture of *i*-octane/oxygen and inert gas. It is of variable composition, such that autoignition of it can be studied after compression over a variable range of compression temperature,  $T_c$ , ranging between 640 and 930 K.
2. Reaction propagation was observed optically with different compression temperatures  $T_c$ , and pressures were measured simultaneously. Initially, at  $T_c = 640$  K, reactive propagation was through a slightly wrinkled laminar flame. As the radius increased propagation soon became predominantly autoignitive with increasing temperature.
3. Propagation entered the *i*-octane NTC regime. Within it, where the gradient of ignition delay time with respect to temperature was minimal, a high autoignitive speed peaked at 323 m/s, with  $T_c = 740$  K.
4. There was no direct influence of the NTC upon detonation.
5. After leaving the NTC regime, with the increasing temperature and pressure, the autoignition velocity again increased, this time with the generation of increasingly strong acoustic waves and ultimate entry into the Detonation Peninsula.
6. The amplitude of the normalised pressure oscillations,  $\Delta P/P$ , increased sharply with increasing values of  $\beta = (\varepsilon/\xi)$  as detonations began to develop.
7. Increasing values of  $\Delta P/P$  with those of  $\beta$  trace the major stages in the evolution of reaction propagation from laminar flame to super-knock.

## Author Contributions

Derek Bradley: Conceptualization, Methodology, Investigation, Review, Editing, and Supervision.  
Jinzhou Li: Formal analysis, Investigation, Methodology, Validation, Visualisation and writing.

## Nomenclature

$a$  acoustic velocity (m/s)

$u_a$  autoignitive velocity (m/s)

$u_l$  laminar burning velocity (m/s)

$S_a$  computed autoignitive speed (m/s)

$S_l$  laminar flame speed (m/s)

$S_m$  measured propagation speed (m/s)

$T_c$  end of compression temperature (K)

$T$  temperature (K)

$\tau_e$  chemical excitation time ( $\mu s$ )

$\tau_i$  ignition delay time (ms)

$r$  radial distance along the hot spot (mm)

$r_0$  hot spot radius (mm)

$r_b$  equivalent radius of burned area (mm)

$P$  pressure (MPa)

$\Delta P$  pressure amplitude (MPa)

$\zeta = a/u_a$ , autoignitive parameter

$\varepsilon = \frac{r_0}{a\tau_e}$ , excitation factor

$\beta = (\varepsilon/\zeta)$  detonation parameter

## 1. Introduction.

Ideally, an RCM, compresses a reactive mixture very rapidly. It then resides motionless, with no heat loss until it autoignites, uniformly, as in a thermal explosion. This enables an autoignition delay time to be measured from the observed characteristics, such as those shown in Fig. 1.

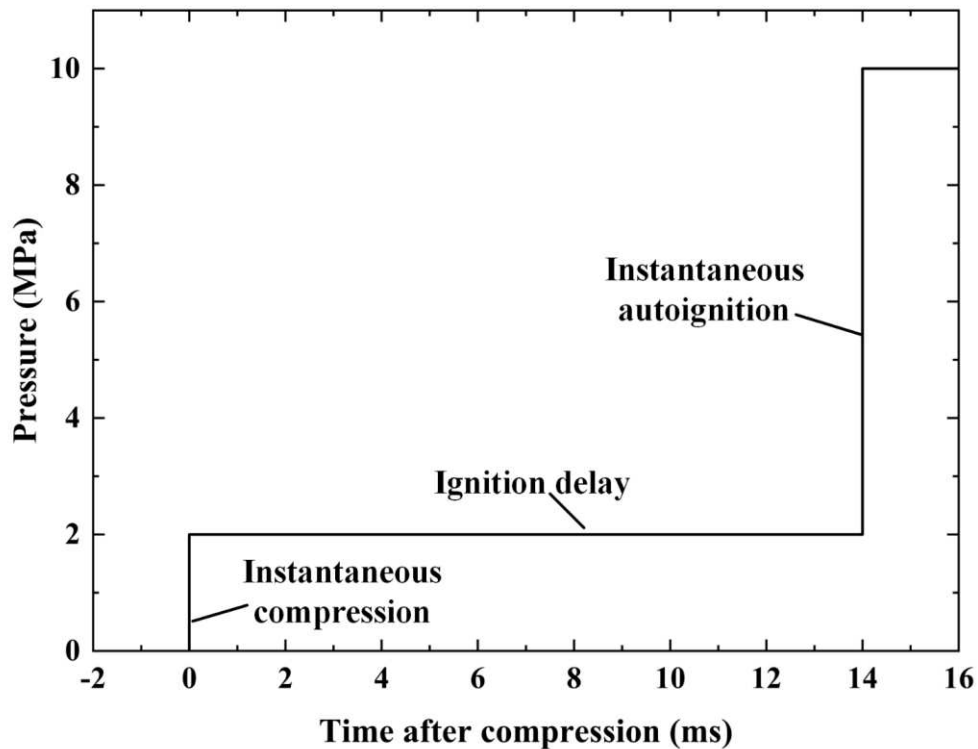


Fig. 1. Idealised Rapid Compression Machine Pressure-time characteristic.

In practice, compression is insufficiently rapid, roll-up vortices are generated by the piston motion, there is heat loss and chemical reaction, during, and after, compression. These and other important aspects of RCMs have been critically reviewed by Sung and Curran in [1].

Another study [2] investigated the differing consequences of chemical reaction during the compression in different RCMs. The present study is of the different reaction propagation modes that occur in the cylinder after compression, prior to the rapid rise in pressure that marks the end of the autoignition delay. The different propagation modes include laminar flame and autoignitive propagation, including a NTC regime. These modes can be followed by the generation of acoustic waves, that can lead to mild or strong detonative propagation.

A theoretical aid to the understanding of these modes and ultimate detonation is provided by the detonation peninsula, within which detonation might occur [3]. The coordinates of the peninsula are:

$\zeta$ , the ratio of the acoustic velocity,  $a$ , to the autoignitive velocity,  $u_a$ , and  $\varepsilon$ , the ratio of the residence time of the developing acoustic wave in a hot spot, to the excitation time,  $\tau_e$ , for the chemical heat release rate. These parameters can indicate the different reaction propagation modes. They have been used to assess the nature of knock in engines and identify the super-knock regime [4], the closest approach to near-instantaneous autoignition. More recently, the  $\zeta - \varepsilon$  parameters have been employed by Liu et al. [5] in their spark ignited RCM studies of stoichiometric *i*-octane/oxygen flame propagation.

The present RCM study is of the diverse reaction modes that can be precursors to detonative autoignition. The changing modes in a cylindrical reaction chamber, were viewed through a high strength optical window, and a high-speed camera system that recorded the initiation, propagation, and transformation of reactions. Pressures were measured with a pressure transducer. In order to study the effects of an NTC regime, following Wei Liu et al. [5], a stoichiometric mixture of *i*-octane and O<sub>2</sub> with variable proportions of different inert gases, N<sub>2</sub>, Ar, and CO<sub>2</sub> was employed. The pressure, was always 2.0 MPa at the end of compression, but the temperatures,  $T_c$ , varied between 640 K and 930 K, dependent upon the concentrations of the inert gases. However, Liu et al. [5] did not observe the unique behaviour of NTC, due to the use of spark ignition for flame generation. Similarly, Gorbatenko et al. [6], in a combined chemical kinetic modelling and RCM study of the anti-knock effects of *n*-butanol, were able identify regimes of subsonic autoignition and deflagration. Robert et al. [7], have employed LES simulation, in combination with the  $\zeta - \varepsilon$  diagram, to predict the transition from deflagration to detonation, in a downsized spark ignition engine.

## 2. Experimental Details

The RCM was originally designed and built in 1968 by Affleck and Thomas [8] at the Shell Thornton Research Centre, and later acquired by the University of Leeds. More recently, it was modified to give optical access to the combustion chamber of 4.5 cm diameter, and 2.15 cm length after compression. A 6.9 cm diameter, 4.0 cm thick, quartz optical window gave a full view. The rig configuration is shown in Fig. 2. It is comprised of a combustion chamber, a hydraulic damping chamber, pneumatic driving, and a mixing chamber.

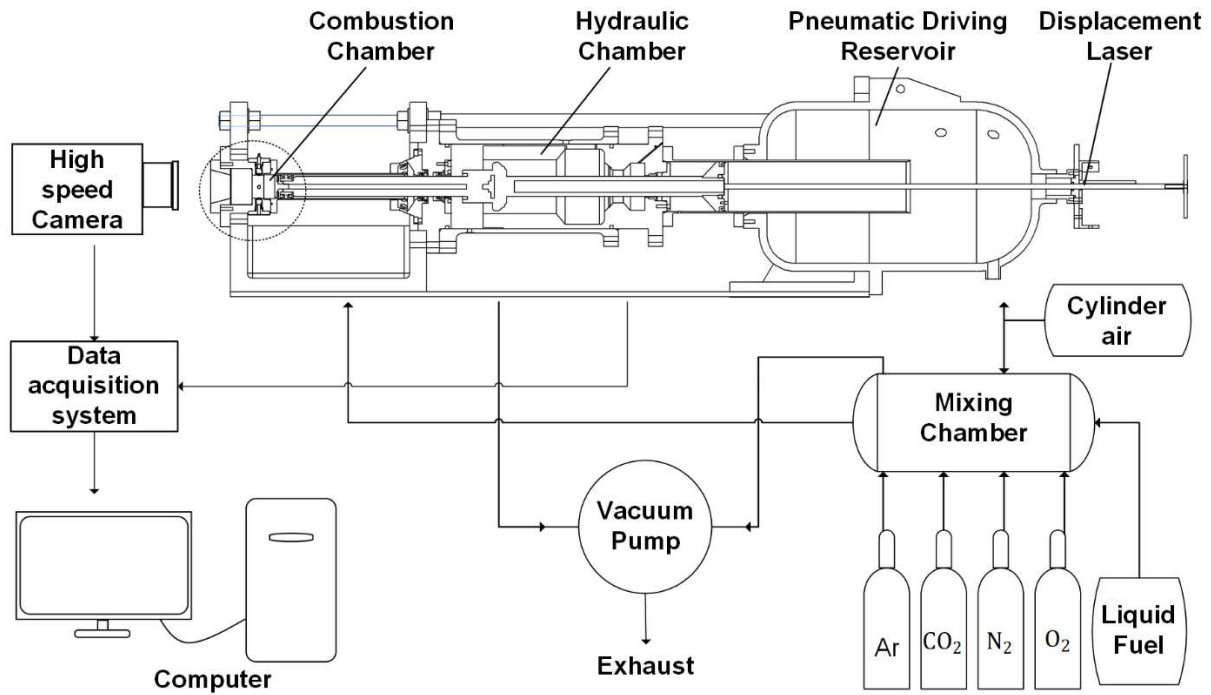


Fig. 2. Layout of the RCM Rig.

The *i*-octane, oxygen and inert gases were mixed inside a 1.8 L heated stainless steel mixing chamber, using partial pressures, and left for two hours to achieve homogeneity. For each compression, the combustion chamber was evacuated. The pneumatic driving reservoir contained air at 1.35 MPa to drive the piston. The mixture within the mixing chamber was transferred to the combustion chamber, where the compression process was completed in 18 ms. The hydraulically damped chamber prevented movement of the piston rod as the piston attained its compression position. Oil inside the narrow gap between the damping ring and groove decelerated and stopped the piston rod. The piston movement during compression was recorded by a Keyence LK-G32 linear displacement laser system. The optical combustion chamber is shown in Fig. 3. It was modified for the present study by the introduction of a high strength quartz window. Pressure was measured with a Kistler dynamic pressure transducer (Kistler; 6045A) coupling, mounted on the combustion chamber wall, with a charge amplifier (Kistler; 5015A) and recorded at a sampling rate of 100 kHz.

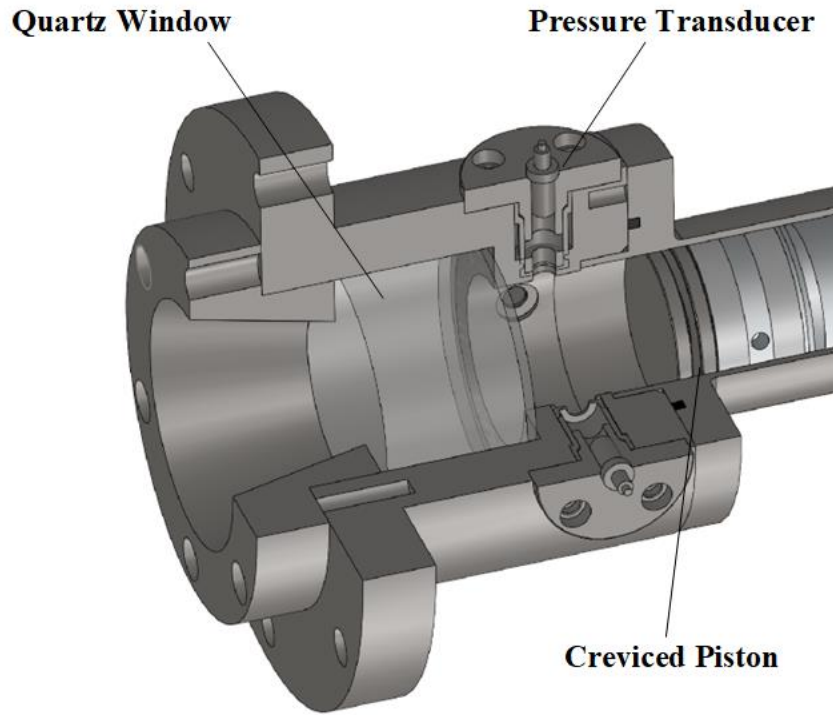


Fig. 3. Optical combustion chamber.

The reaction front was visualised from the flame's radiative emissions. A high-speed camera (Photron SA1.1) with a 100 mm lens (Tokina AT-X PRO 1:2.8D), in front of the quartz window, recorded images with a two-dimensional resolution of 256 x 256 pixels and pixel size of 0.176 mm/pixel. The framing rate was 67,500 frames per second, with the shutter speed maintained at 14.81  $\mu$ s. The camera was triggered by the piston displacement signal, 13 mm before the piston reached the end of compression. It was estimated that the system could detect kernel temperatures above 2500 K.

All images were post-processed by the MATLAB program [5, 9, 10], with a "binarising-thresholding" technique [11] to define the reaction volume characteristics. Radiation images were loaded by the MATLAB code to form a matrix of pixel numbers. These were binarized for an optimal threshold level, effectively identifying the majority of burned areas with high precision. Those with an intensity above the threshold were classed as burned. The burned mass fraction, BMF, was defined as the fraction of total pixels that were burned.

Figure 4 shows seven pairs of images, recorded during the explosion of a mixture compressed to a temperature,  $T_c$  of 810 K. The lower row shows raw, monochrome, data, whilst the top row shows the better contrasting binary images, derived from the thresholding technique. Clear white areas indicate

burned gas. Propagation speeds,  $S_m$ , were measured, along with the pressure. The value of  $S_m = \frac{dr_b}{dt}$  is calculated by evaluating the expansion of the burned area, which is occupied by combustion gases in the combustion chamber, where  $r_b$  represents the equivalent radius of the burned area.

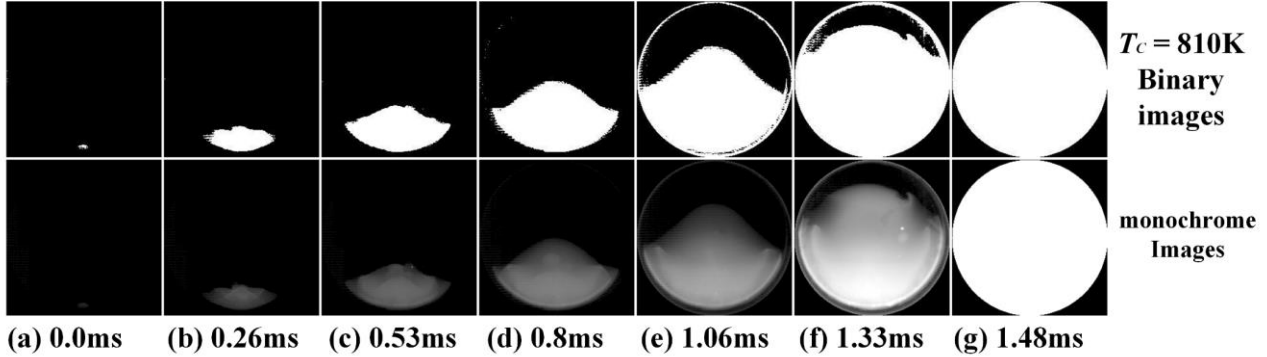


Fig. 4. White images of burned gas, using the binarising-thresholding technique.

The eleven different mixtures of stoichiometric *i*-octane and oxygen had different values of  $T_c$ , due to the differing concentrations of the inert diluents. Pressures were measured continually and temperatures were implied from these, using the isentropic relationship, with ratios of specific heats, obtained from the GasEq code [12]. All mixtures were stoichiometric, with constant mole fractions of *i*-octane and  $O_2$ , of high purity (>99.99%). They were prepared in the mixing chamber at 350 K and left for two hours to attain homogeneity. Compositions of all eleven mixtures and their temperatures after compression,  $T_c$ , are given in Table 1. Pressures at the end of compression were always 2.0 MPa. Examinations of the flame images and pressure records showed different modes of reactive propagation, indicated in the second column. These include:

Laminar burning,  $L$ , autoignitive propagation,  $A$ , generation of pressure pulses,  $P$ , of increasing strength and, ultimately, initiation of detonation and full detonation,  $D$ . There were five instances in which an explosion terminated with a detonation.

Table 1. Mixture Compositions, and compression Temperature,  $T_c$ , Different compression temperatures were obtained by varying mole fractions of the three inert additives. Compression was to 2.0 MPa.

Mixture Composition Mole Fractions (%)							
$T_c$	Mode	$\tau_i$ (ms)	<i>i</i> -octane	$O_2$	$N_2$	Ar	$CO_2$
640	$L$	52.3	1.65	20.66	18.62	0	59.2
670	$A$	26.3	1.65	20.66	38.23	0	39.4

690	<i>A</i>	19	1.65	20.66	47.1	0	30.6
710	<i>P, A</i>	14.7	1.65	20.66	58.9	0	18.8
740	<i>P, A</i>	15.5	1.65	20.66	67.8	0	9.9
770	<i>P, A</i>	16.1	1.65	20.66	77.7	0	0
790	<i>P, D</i>	16.5	1.65	20.66	65.9	11.8	0
810	<i>P, D</i>	17.6	1.65	20.66	56.1	21.6	0
830	<i>P, D</i>	21.3	1.65	20.66	48.2	29.5	0
900	<i>P, D</i>	11.7	1.65	20.66	21.6	56.1	0
930	<i>P, D</i>	7	1.65	20.66	11.8	65.9	0

### 3. Different Properties of the Mixtures

Six different properties are considered.

#### 3.1 Laminar Burning Velocity

It was not easy to obtain accurate propagation velocities in an RCM, but theoretical values were possible. The possibility of obtaining near-stoichiometric laminar burning velocities was always checked. These were calculated using a freely propagation laminar flame model in CHEMKIN software [13], incorporating the *i*-octane oxidation kinetics found in the detailed Lawrence Livermore National Laboratory (LLNL) gasoline surrogate chemical kinetics [14]. The expansion of the burned gas creates a flame speed equal to the laminar burning velocity,  $u_l$ , multiplied by the ratio of unburned to burned gas density. The effects of temperature on the unburned to burned density ratio are considered in this study. Relative to air, CO<sub>2</sub> dilution notably decreases the laminar burning velocity. With  $T_c$  values of 640 K, 670 K, and 690 K, the impact of CO<sub>2</sub> on the laminar burning velocity is considered.

The values of  $u_l$  obtained from the LLNL gasoline surrogate chemical kinetics are shown in Fig. 5 at different temperatures, with pressures of 0.1 and 2.0 MPa. An empirical expression in [15] for the dependency on temperature and pressure of the laminar burning velocity is in the form:

$$u_l = 1.363 \left( \frac{T}{640} \right)^{2.2} \left( \frac{P}{0.1} \right)^{-0.27}, \quad (1)$$

with  $T$  in K and  $P$  in MPa. The dashed lines in Fig. 5 demonstrate this expression provides good fits to the computed data. The laminar flame speed, derived from Eq. (1) multiplied by the density ratio,

is used in Sections 4.1 and 4.2 for comparison with measured and calculated autoignitive speeds.

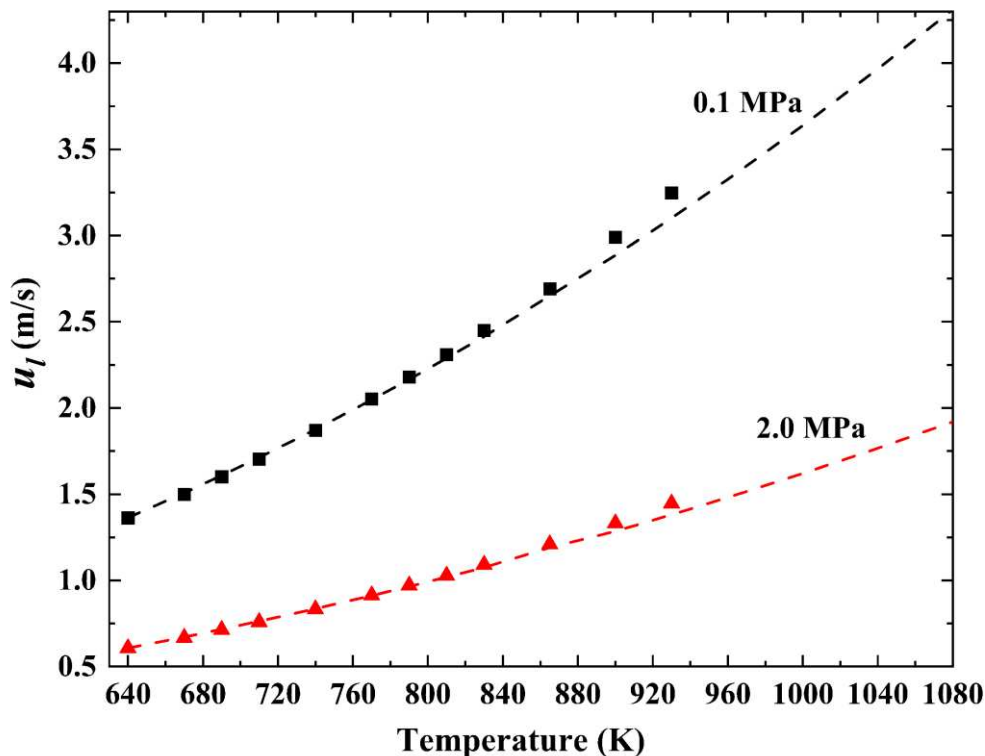


Fig. 5. Maximum laminar burning velocity calculated from LLNL gasoline chemical kinetics [14] of *i*-octane/air at 0.1 MPa and 2.0 MPa. More empirically the data were extended to higher temperatures and pressure using Eq. (1).

### 3.2 Autoignition Delay Time

Autoignitive propagation speeds are dependent upon autoignition delay times,  $\tau_i$ . These were measured in the RCM at the different compression temperatures,  $T_c$ , and are shown in Fig. 6. The extent of the NTC regime is indicated from 725 K to 830 K. Within it, the value of  $\tau_i$  increases with temperature. The compositions of mixtures and their  $T_c$  values are listed in Table 1. Figure 6 also includes the measured  $\tau_i$  values from different RCMs of stoichiometric *i*-octane at 2.0 MPa [16]. The current measurements are in satisfactory agreements with the additional data of others.

The filled triangle symbols in Fig. 7 are the values of  $\tau_i$  derived from the current measurements, corresponding to 2.0 MPa and kinetically, modelled values from CHEMKIN software [13] with detailed LLNL gasoline surrogate chemical kinetics [14] at 2, 4, and 10 MPa, and at temperatures between 640 K and 1200 K. Chemical kinetically, there was a close similarity between the current experimental mixtures and the stoichiometric *i*-octane/air mixtures.

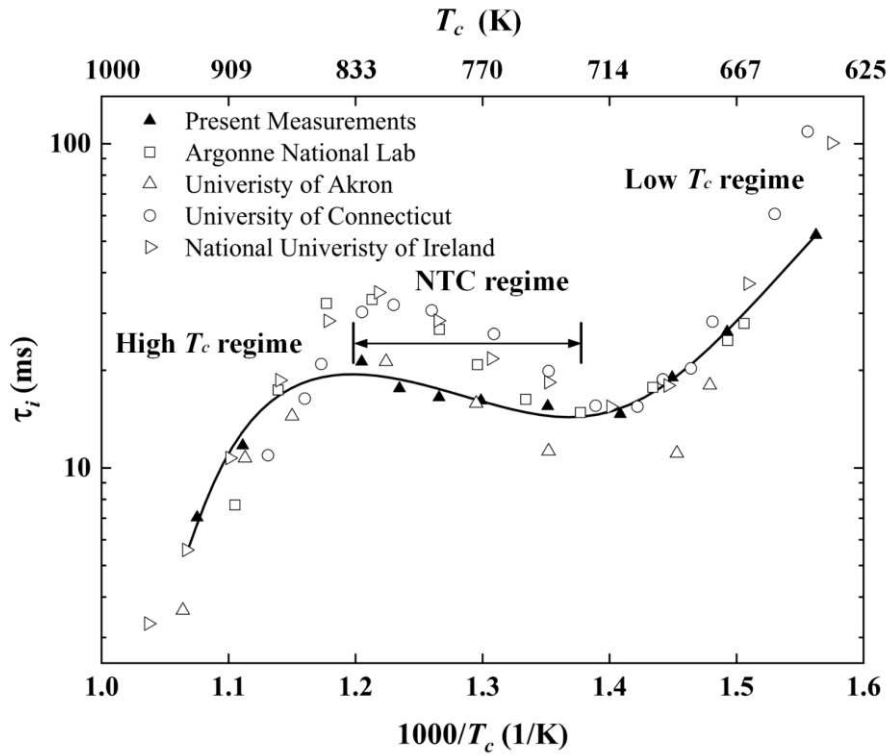


Fig. 6 Currently RCM measured values of  $\tau_i$  for stoichiometric *i*-octane/oxygen mixtures, compressed to 2 MPa with  $T_c$  values between 640 and 930 K, as listed in Table 1. Additional data are from the 2nd International RCM Workshop [16].

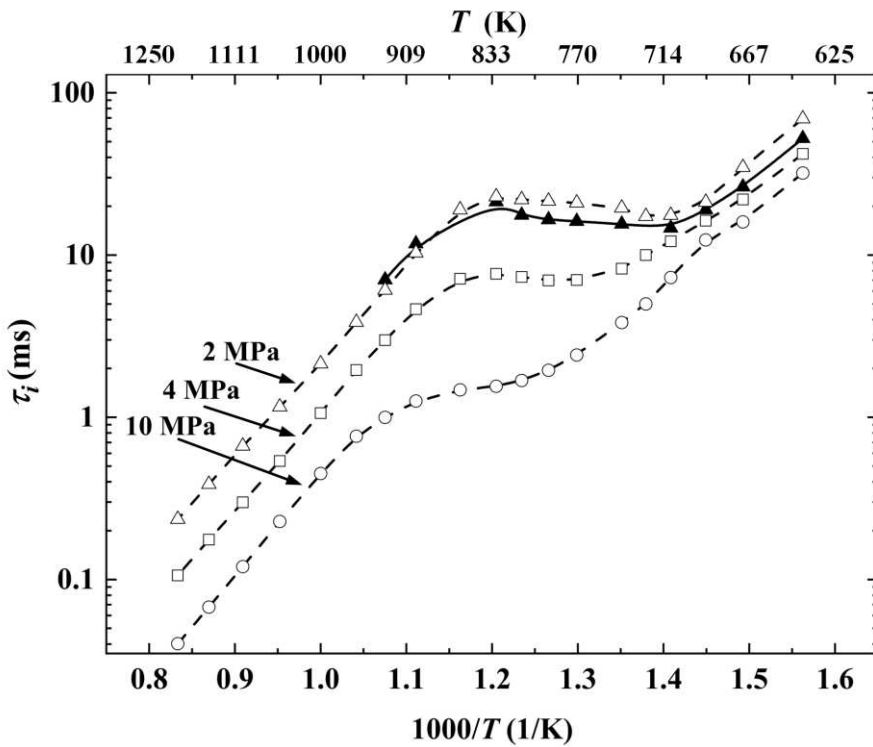


Fig. 7. Values of  $\tau_i$  for stoichiometric *i*-octane/oxygen inerts for current experiments at 2 MPa and *i*-octane/air chemical kinetic values at 2, 4, and 10 MPa.

### 3.3 Autoignitive Velocity

For autoignitive propagation, the autoignitive velocity,  $u_a$ , is, albeit somewhat empirically:

$$u_a = \frac{\partial r}{\partial \tau_i} = \left(\frac{\partial r}{\partial T}\right)\left(\frac{\partial T}{\partial \tau_i}\right). \quad (2)$$

The autoignitive propagation speed,  $S_a$ , is  $u_a$  multiplied by the same density ratio as for the flame speed. In a hot spot, the temperature decreases with distance from the centre, resulting in a negative derivative of  $\left(\frac{\partial r}{\partial T}\right)$ . Concurrently,  $\tau_i$  decreases as the temperature increases, yielding a negative  $\left(\frac{\partial T}{\partial \tau_i}\right)$ , which leads to a positive  $u_a$ . In contrast, under NTC conditions,  $\tau_i$  increases with rising temperature, giving a positive  $\left(\frac{\partial T}{\partial \tau_i}\right)$ . In this regime, cool spots are expected to ignite in areas of lower temperature that have a positive  $\left(\frac{\partial r}{\partial T}\right)$  [17]. Therefore, with NTC,  $\left(\frac{\partial r}{\partial T}\right)$  remains positive, and at a cold spot,  $\left(\frac{\partial r}{\partial T}\right)$  is positive and  $u_a$  is positive. Measuring the temperature gradient around a hot or cool spot poses a significant challenge, with precision often being unattainable. Kalghatgi and Bradley [18] assumed a constant temperature gradient of  $\frac{\partial T}{\partial r} = -2\text{K/mm}$  for a hot spot, chosen for its strong correlation with experimental engine findings. This assumption has been widely implemented in studies [3, 4, 6].

Momentarily, from Eq. (2), a NTC can generate values of  $\left(\frac{\partial \tau_i}{\partial T}\right)$  that are close to, or even equal to, zero, with implied infinite, or very large values of  $u_a$ . Eq. (2) is indeed a key equation, particularly if it is inside the NTC regime, when due account must be taken of a difficulty of ultra-high values of  $u_a$ . Otherwise, there is some evidence of the reliability of Eq. (2). Numerically,  $\tau_i$  was empirically approximated by following the methodology in [4], using multiple regression based on the chemical kinetics predicted values in Fig. 7. Temperature and pressure were employed as independent variables across the three regimes.

For the Low Temperature Regime (640 K to 725 K):

$$\tau_i = 1.31 \times 10^{-4} \times e^{\left(\frac{8231}{T}\right)} \times \left(\frac{P}{2}\right)^{-0.3}, \quad (3)$$

$$\partial \tau_i / \partial T = -8231 \times \tau_i / T^2, \quad (4)$$

For the NTC Regime (725 K to 830 K):

$$\tau_i = 1.81 \times e^{(0.0029 \times T)} \times \left(\frac{P}{2}\right)^{-1.2}, \quad (5)$$

$$\partial \tau_i / \partial T = 0.0029 \times \tau_i, \quad (6)$$

For the High Temperature Regime (beyond 830 K):

$$\tau_i = 5.59 \times 10^{-6} \times e^{(13003/T)} \times \left(\frac{P}{2}\right)^{-1.15}, \quad (7)$$

$$\partial\tau_i/\partial T = -13003 \times \tau_i/T^2, \quad (8)$$

With  $\tau_i$  in ms,  $P$  in MPa and  $T$  in K.

Eq. (2) shows the crucial importance of  $\frac{\partial\tau_i}{\partial T}$  and Fig. 8 shows a plot of  $\frac{\partial\tau_i}{\partial T}$  for stoichiometric *i*-octane/air against temperature at pressures of 2, 4 and 10 MPa. The value increases with the temperature, approaching zero in the NTC regime, then becomes slightly positive.

The values of  $\frac{\partial\tau_i}{\partial T}$  in Eqs. (4), (6) and (8) are employed in Eq. (2) to derive  $u_a$ . These values, along with the acoustic velocity, are illustrated in Fig. 9. The expression for  $u_a$ , and the possible closeness of the value of  $\frac{\partial\tau_i}{\partial T}$  to zero, creates an abnormally amplified sensitivity of the value of  $u_a$ , with a near zero  $\frac{\partial\tau_i}{\partial T}$  leading to a very high  $u_a$ . The problem is compounded with the uncertainty about the assumed constant value of  $\frac{\partial r}{\partial T}$ . Figure. 9 shows that, initially,  $u_a$  is very small but increases with temperature on entering into the NTC regime, only to fall in value on leaving it for the high temperature regime. There, with increasing temperature, there is a sharp increase in  $u_a$ , particularly at high pressure. Values of  $u_a$  derived by this method, are applied in Section 4.1 to enable the autoignitive speeds associated with the pressure trace to be found. This is also utilised to ascertain the dimensionless parameter,  $\zeta$  for the Detonation Peninsula.

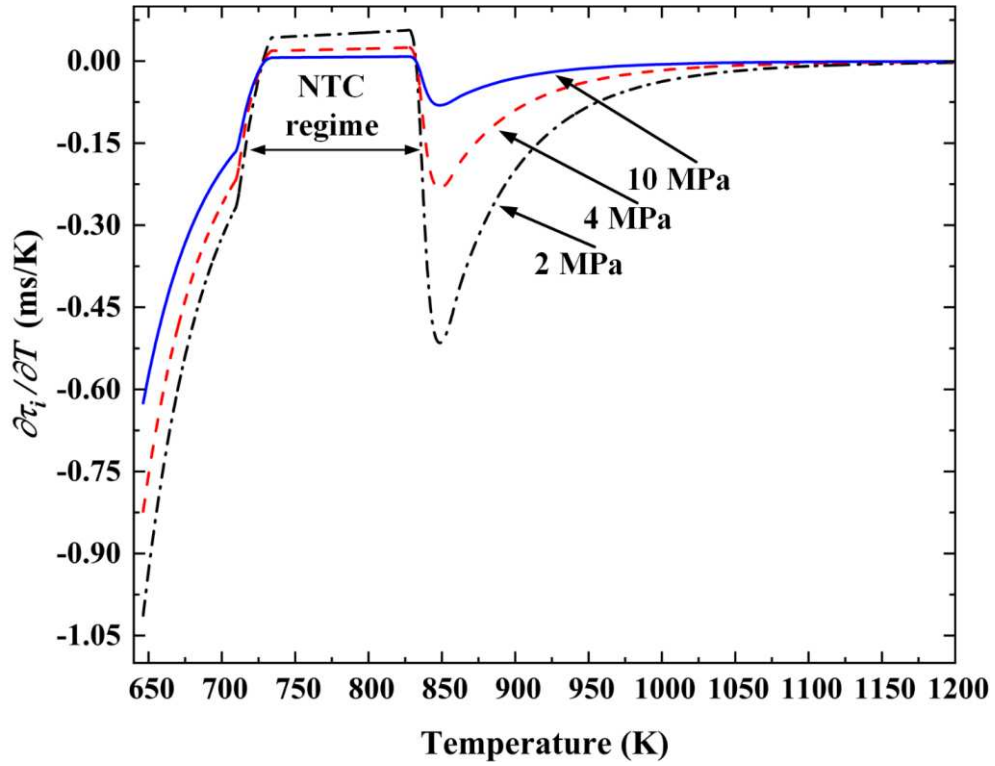


Fig. 8. Values of  $\partial\tau_i/\partial T$  for stoichiometric *i*-octane/air, derived from chemical kinetic values at 2, 4 and 10 MPa.

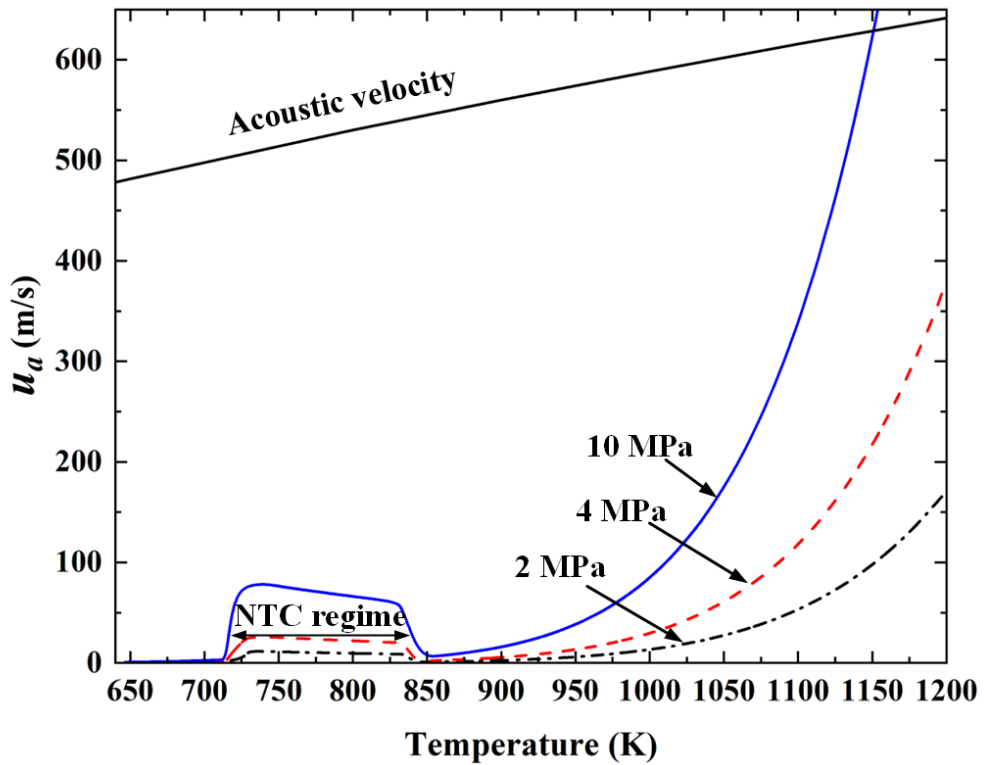


Fig. 9.  $u_a$  for stoichiometric *i*-octane/air derived from chemical kinetic values at 2, 4 and 10 MPa.

### 3.4 Autoignition Parameters, $\zeta$ and $\epsilon$ .

The closeness of the autoignitive velocity  $u_a$ , to the acoustic velocity,  $a$ , is relevant to the development of a detonation, and the autoignitive parameter,  $\zeta$ , the ratio  $a/u_a$ . The related excitation factor,  $\varepsilon$ , expresses how rapidly an acoustic wave can be accelerated by chemical energy gained at the hot or cold spot of the chemical energy. The residence time of the acoustic wave at a hot or cold spot of radius  $r_o$ , is,  $r_o/a$  and the excitation time for the greatest heat release rate is  $\tau_e$ . If the chemical heat release time is short enough into the wave, it will reinforce it. The relevant parameter is the excitation factor,  $\varepsilon = \frac{r_o}{a\tau_e}$ . Following [3, 4, 6] a hot spot radius of  $r_0 = 5$  mm is assumed. The value of acoustic velocity,  $a$ , is obtained from the GasEq code [12]. It later will be shown how a low value of  $\zeta$  and a high value of  $\varepsilon$  are conducive to a detonation.

Fig. 10 shows values of  $\zeta$  for stoichiometric *i*-octane/air at different temperatures and pressures of 2, 4, and 10 MPa. In the low temperature regime, both increasing temperature and pressure decrease  $\zeta$ . In the NTC regime, the value of  $\zeta$  rapidly decreases due to the gradient,  $\frac{\partial\tau_i}{\partial T}$ , approaching zero. When leaving the NTC regime, it increases. In the high temperature regime, it sharply decreases with increasing temperature. It reaches unity as the temperature reaches 1150 K, and a pressure of 10 MPa.

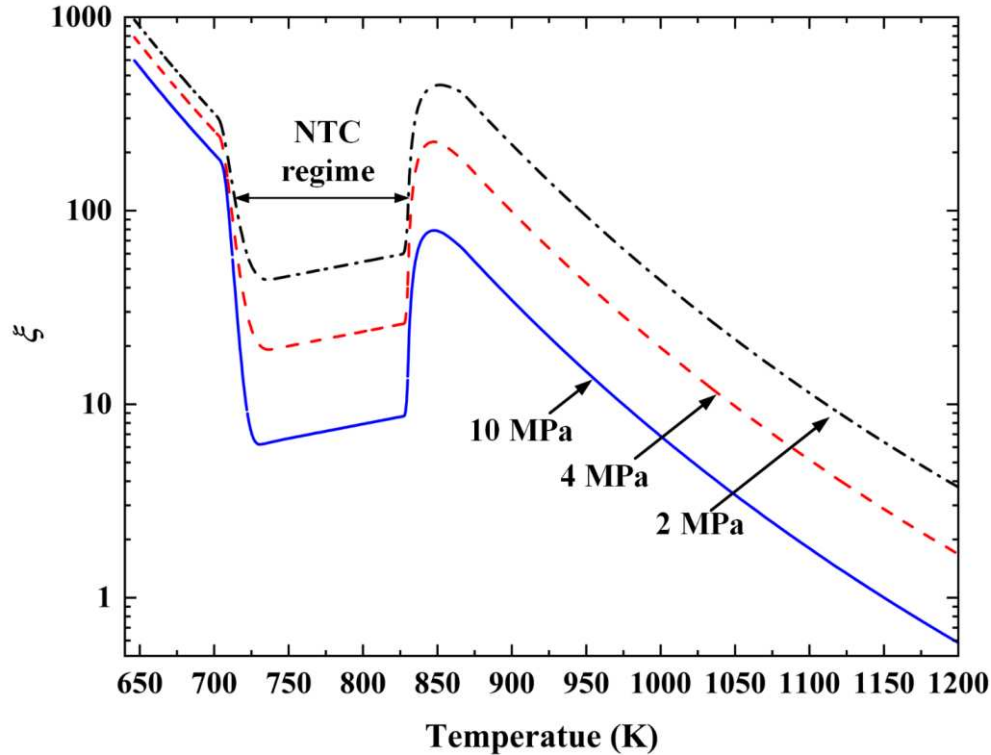


Fig. 10. Values of  $\zeta$  for stoichiometric *i*-octane/air from chemical kinetic values at 2, 4 and 10 MPa.

### 3.5 Chemical Excitation Times, $\tau_e$ .

This is a key parameter in the evaluation of  $\varepsilon$ . It was evaluated using CHEMKIN's closed homogeneous batch reactor [13], with detailed gasoline surrogate chemical kinetics [14], for the *i*-octane/air mixtures. A typical temporal profile of rapid total heat release rates in a constant volume chamber is shown in Fig. 11. Lutz et al. [19] introduced the concept of chemical excitation time,  $\tau_e$ , which refers to the period during which exothermic chemical reactions accelerate and rapidly release thermal energy. It is the time interval from the point with 5% of the maximum total heat release rate to the attainment of the maximum value. Very many reactions are involved and at the highest temperatures the chain branching  $\text{H} + \text{O}_2$  reaction is particularly significant.

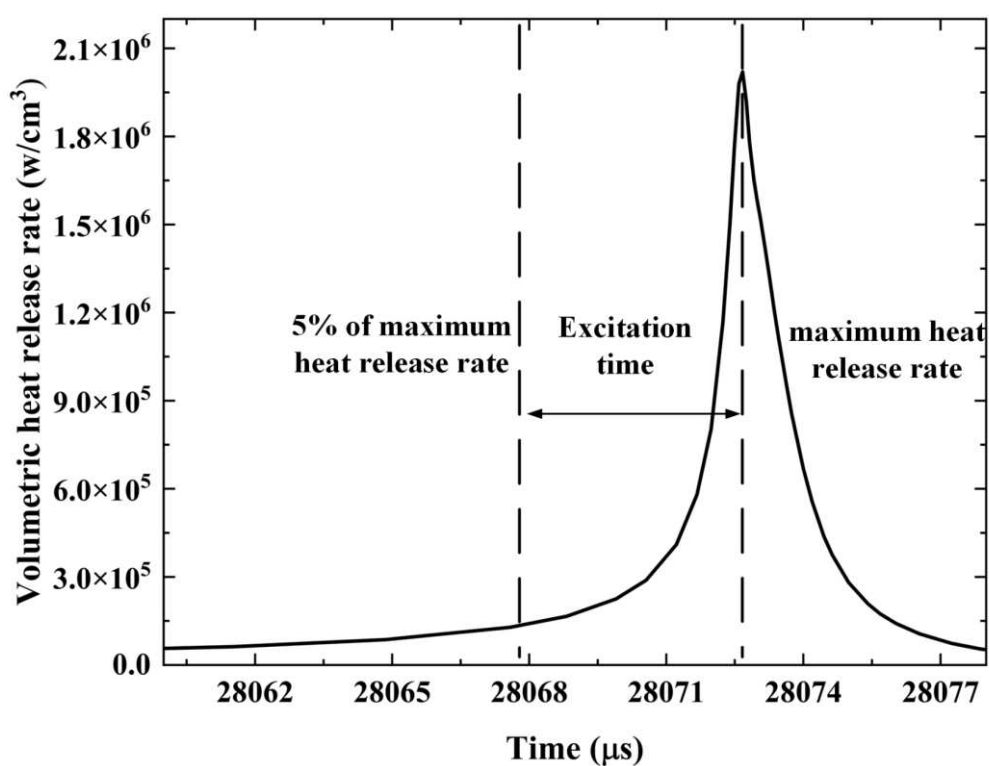


Fig. 11. Total heat release rate for the stoichiometric *i*-octane/air mixtures, at 2 MPa and  $T_c = 830$  K. Values of,  $\tau_e$ , found in this way at different value of temperatures and pressure are shown in Fig. 12.

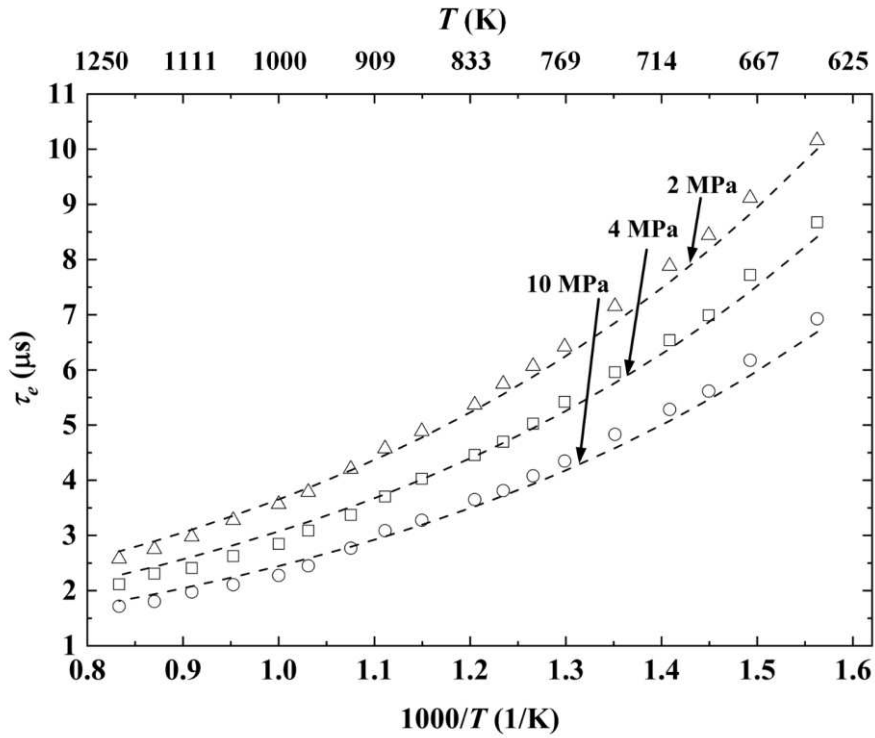


Fig. 12. Computed chemical excitation times,  $\tau_e$ , for stoichiometric *i*-octane/air mixtures plotted against  $1000/T$ , at 2, 4 and 10 MPa.

Numerically, an empirical expression for the dependence of  $\tau_e$  on temperature and pressure is:

$$\tau_e = 0.61 \times e^{\left(\frac{1790}{T}\right)} \times \left(\frac{P}{2}\right)^{-0.25}, \quad (9)$$

With  $\tau_e$  in  $\mu\text{s}$ ,  $P$  in MPa and  $T$  in K. The dashed lines are good fits to the temperature and pressure dependencies. Figure. 13 shows the computed values of  $\varepsilon$  for stoichiometric *i*-octane/air as a function of temperature at different pressures.

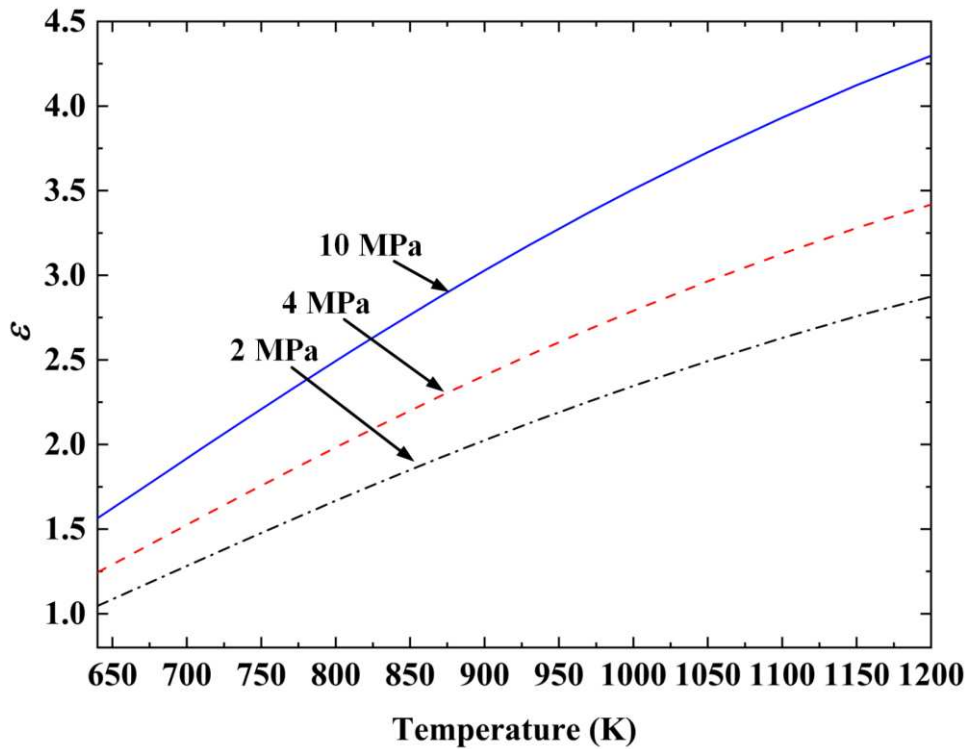


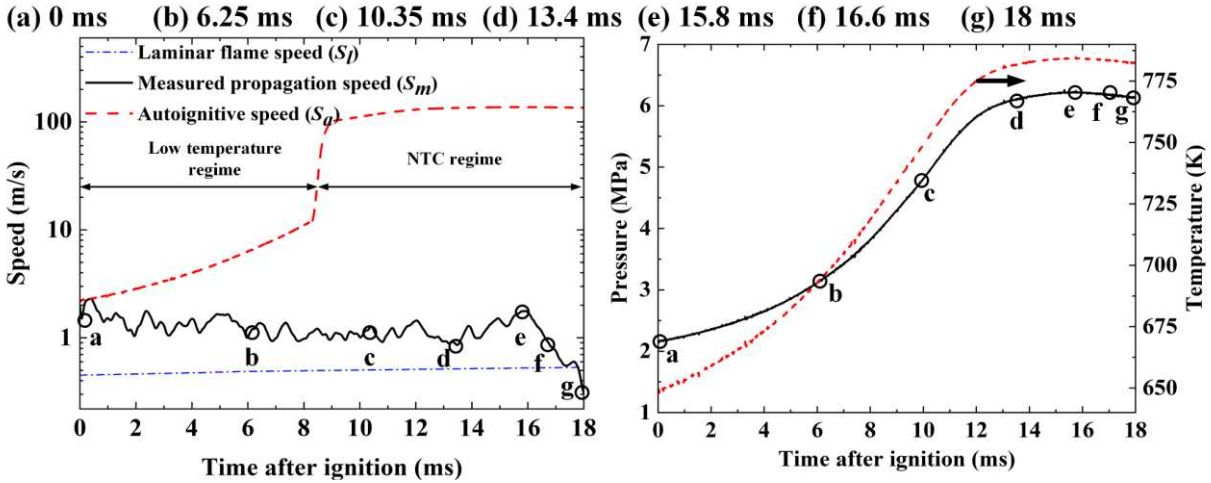
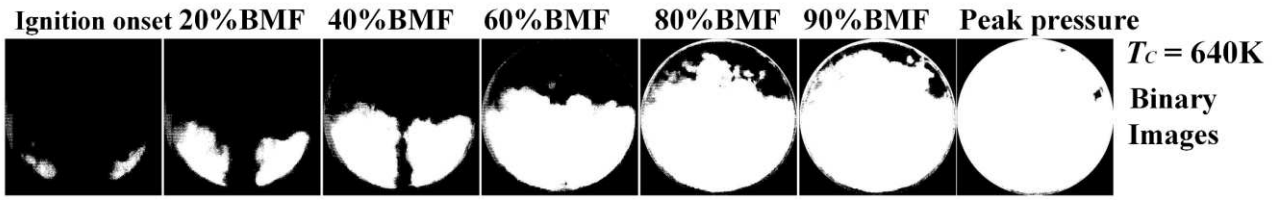
Fig. 13. Values of  $\varepsilon$  for stoichiometric *i*-octane/air derived from chemical kinetic values at 2, 4 and 10 MPa.

#### 4. Reaction after Compression

##### 4.1 Processing of Experimental Images and Measurements

This section describes the processing of the experimental images and measurements of reaction fronts throughout the explosions. Values of  $\frac{\partial \tau_i}{\partial T}$  are required to compute the autoignitive speed for each explosion and its increasing values of  $T$ . Each set of images and measured data, including pressure and temperature, are associated with one of the 11 values of  $T_c$ , such as can be seen in Fig. 14. In all the flame imaging, sequences of binary and monochrome images were obtained, but only the former are shown in this sequence. As detonations eventually develop, slightly additional analytical procedures are adopted. This first sequence starts with the lowest value of  $T_c$  of 640 K. The ensuing propagating reaction waves, usually are initiated close to of the cylinder wall and have a changing velocity. Measured and calculated propagation speeds, are shown on the left, under the images. Measured pressures, and derived unburned gas temperatures are on the right. The associated  $T$  and  $P$  values, enable laminar flame and autoignitive speeds to be calculated. These are shown by the chain-dotted and dashed curves, respectively, on the left.

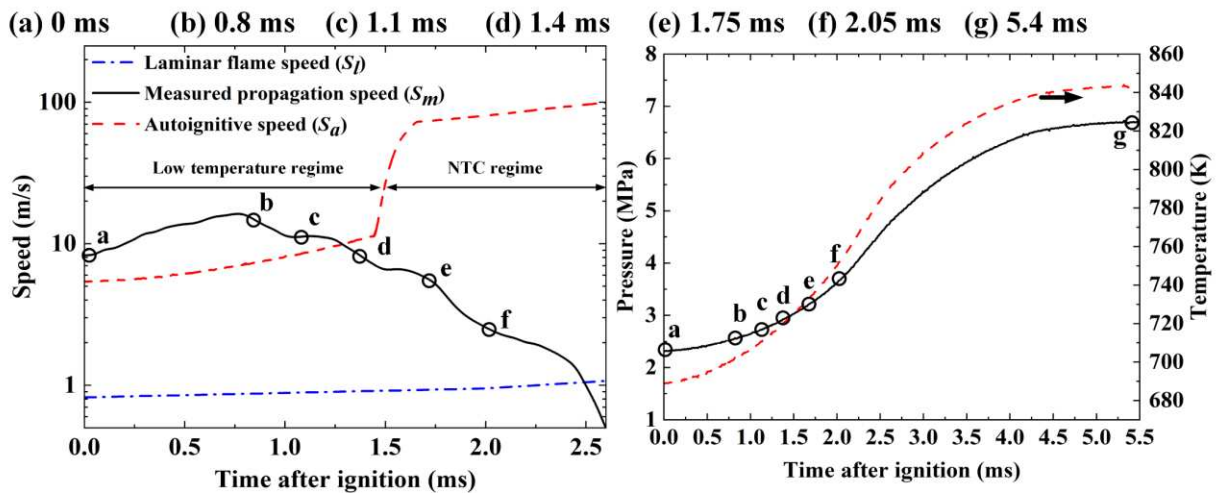
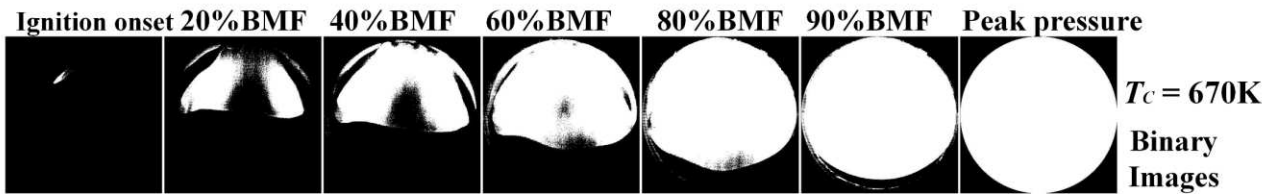
Burned Mass Fractions, BMF, are shown above each binary image. It is assumed there is no combustion in the black area behind the reaction front and the reaction front is the boundary between the burned and unburned regions.



(a) Speeds of Reactive Fronts (b) Pressure and unburned gas temperature profiles

Fig. 14.  $T_c = 640\text{K}$ .

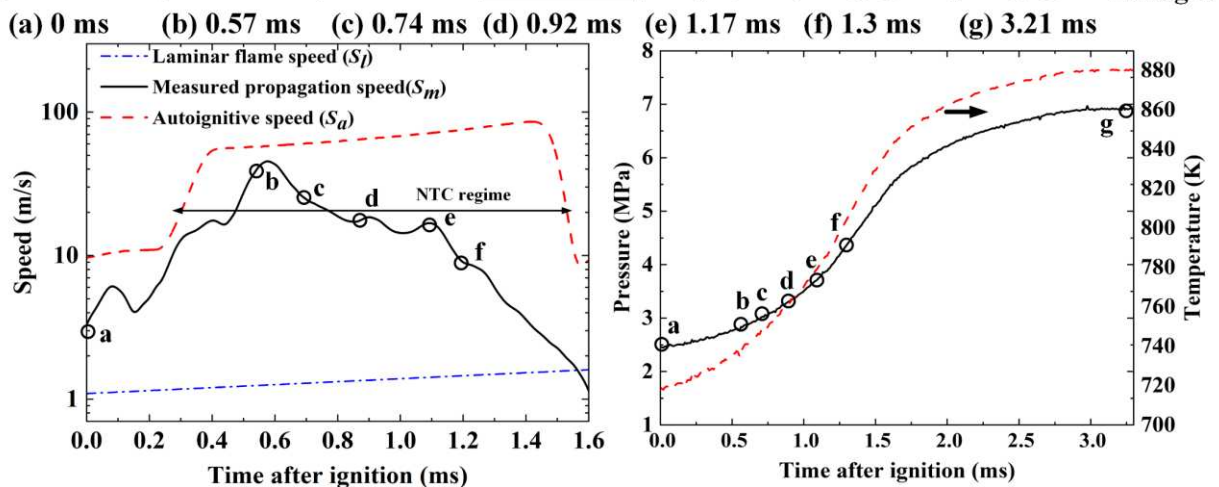
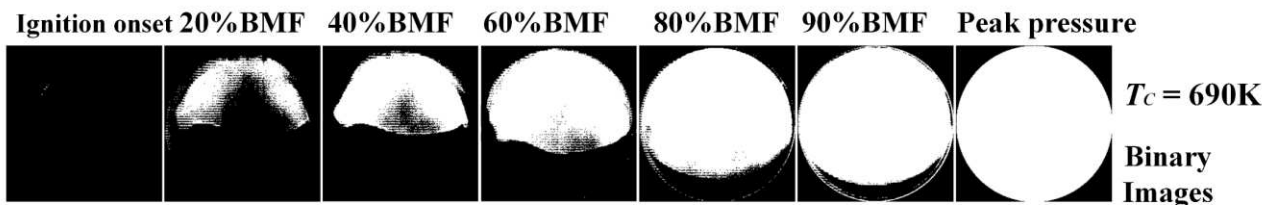
In Fig. 14, binary images from the monochrome high-speed camera initially show two small ignition areas or hot spots, to emerge instantaneously from both left and right at the bottom of cylinder wall and start to propagate towards the centre of chamber. The measured propagation speed,  $S_m$ , is in this instance, fluctuating around 1 m/s, close to the computed laminar flame speed,  $S_l$ , whilst the computed autoignitive speed,  $S_a$ , is significantly higher, suggesting the initial dominance of laminar/turbulent flame propagation. The moderate wrinkling of the propagation front suggests the presence of mild turbulence generated from the compression process. The turbulence-induced wrinkling, which leads to accelerated flame propagation speed, could be the reason the measured propagation speed surpasses the laminar flame speed.



(a) Speeds of Reactive Fronts (b) Pressure and unburned gas temperature profiles

Fig. 15.  $T_c = 670\text{K}$ .

Displayed in Fig. 15, at this higher value of  $T_c = 670\text{K}$ , the first binary image shows a small initiating kernel on the left, to be later joined by one from the right. Initially, values of  $S_m$  are closer to the autoignitive speed,  $S_a$ , computed as described in Section 3.3. The fact that  $S_m$  is considerably greater than the laminar flame speed indicates the presence of an autoignitive propagation mode.



(a) Speeds of Reactive Fronts (b) Pressure and unburned gas temperature profiles

Fig. 16.  $T_c = 690$  K.

In Fig. 16, there are initially two reaction centres that subsequently become closely linked. Briefly, at the start, the measured propagation and calculated laminar flame speed are close. As the temperature enters the NTC regime, the measured propagation speed interacts significantly and generally moves closer to the autoignitive speed. This is the last explosion without significant pressure oscillation.

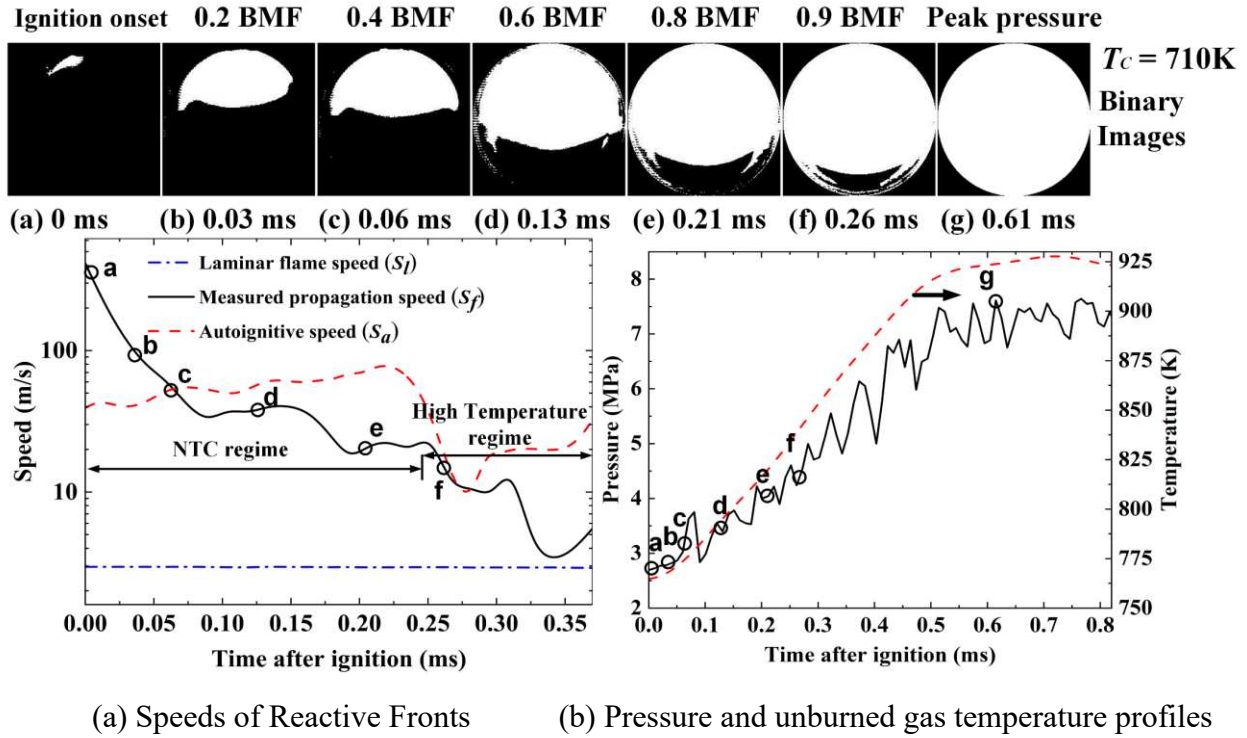
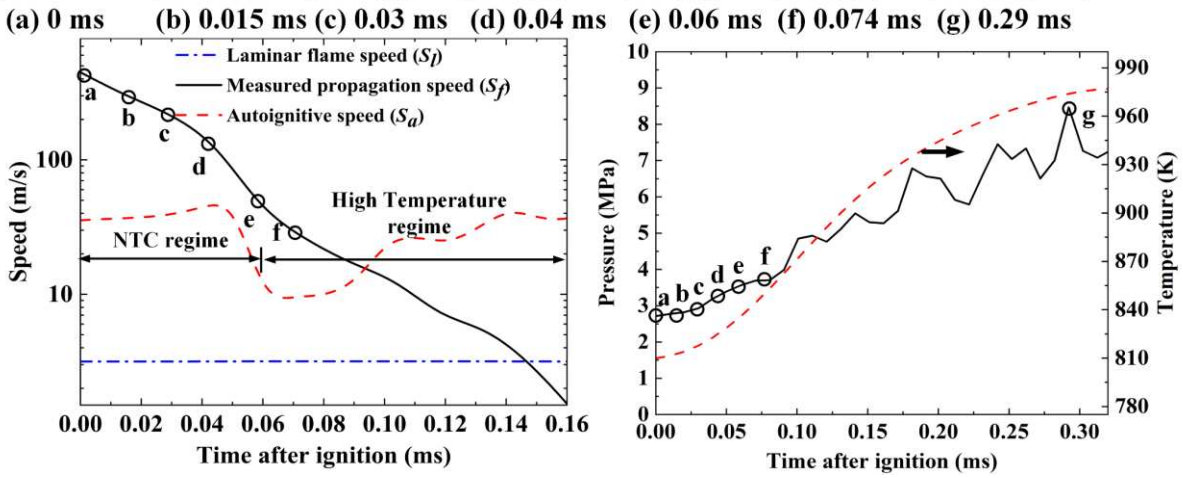
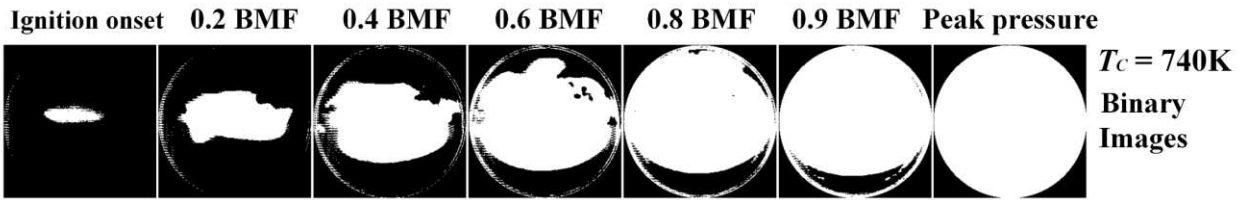


Fig. 17.  $T_c = 710$  K.

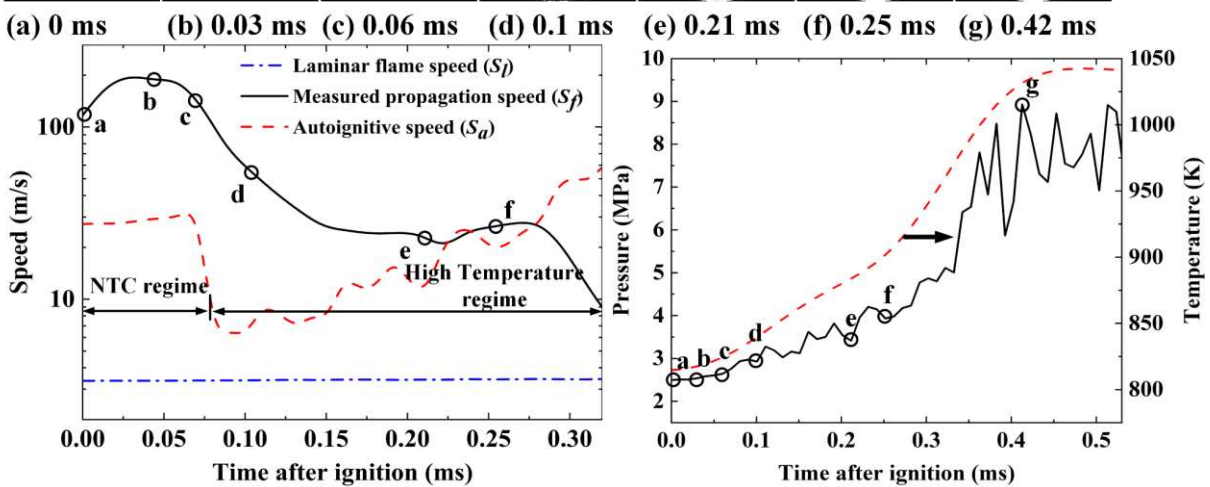
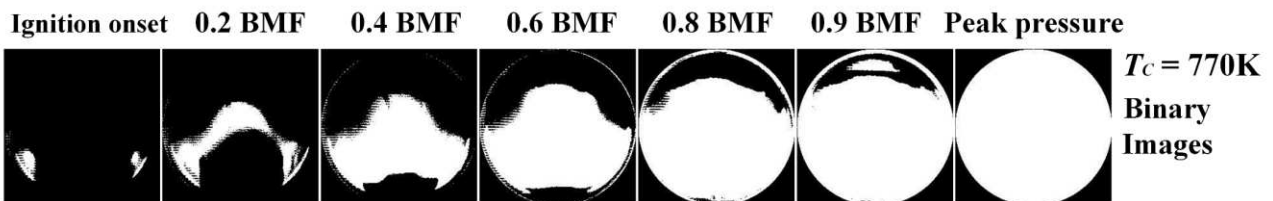
At  $T_c = 710$  K, depicted in Fig. 17, the NTC regime is close at autoignition. Figure 9 suggests a resulting increase in autoignitive speed. This is confirmed by the measured propagation speed. For the first time, significant pressure oscillations are initiated early, and grow in amplitude. A high measured propagation speed of 330 m/s is observed at the onset of ignition.



(a) Speeds of Reactive Fronts      (b) Pressure and unburned gas temperature profiles

Fig. 18.  $T_c = 740\text{ K}$ .

The NTC regime is entered at  $T_c = 740\text{ K}$ . Fig. 18 shows that there is only partial autoignitive computational support for the measured, initially high, but diminishing, propagation speed. A maximum measured propagation speed of 390 m/s is observed at the onset of ignition of a cool spot. There is growth in the amplitudes of pressure fluctuations.



(a) Speeds of Reactive Fronts      (b) Pressure and unburned gas temperature profiles

Fig. 19.  $T_c = 770$  K.

Fig. 19 demonstrates within the NTC regime, there is also a growth in pressure fluctuation amplitudes and high initial measured propagation speeds, with some initial support from autoignitive speed computations.

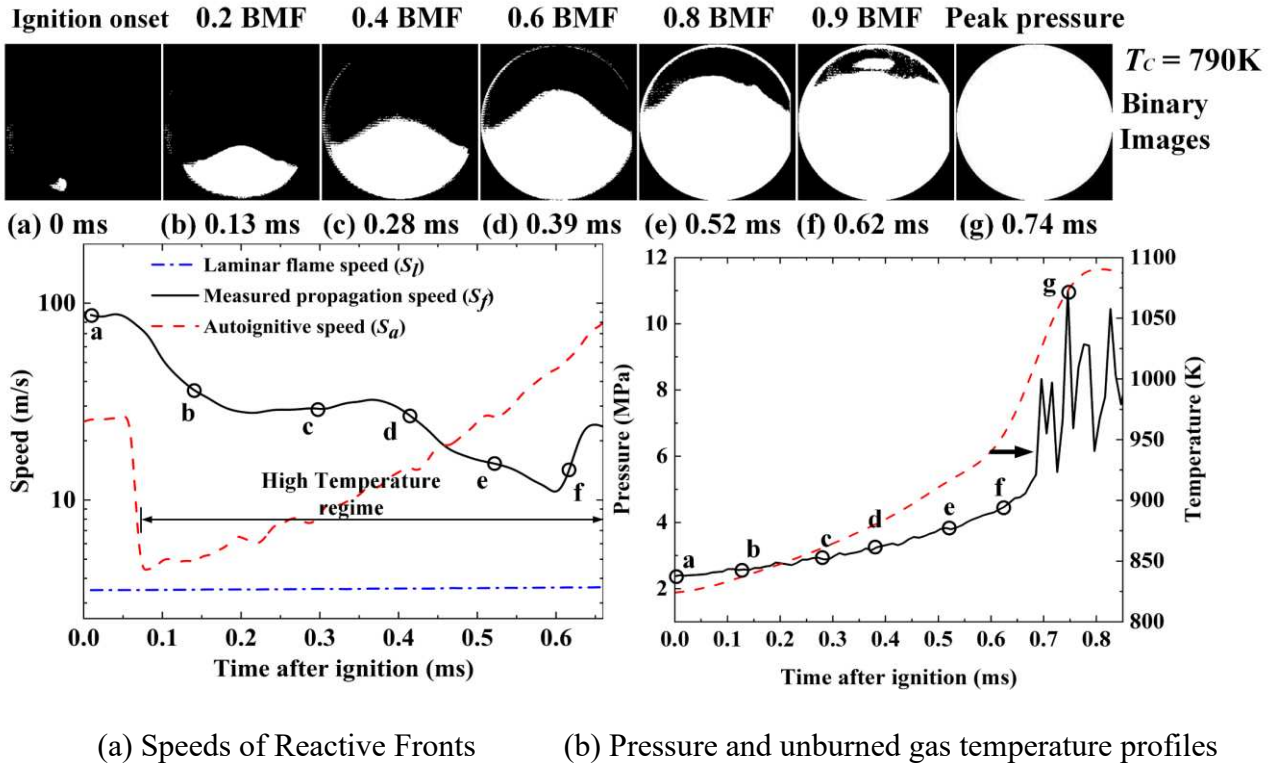
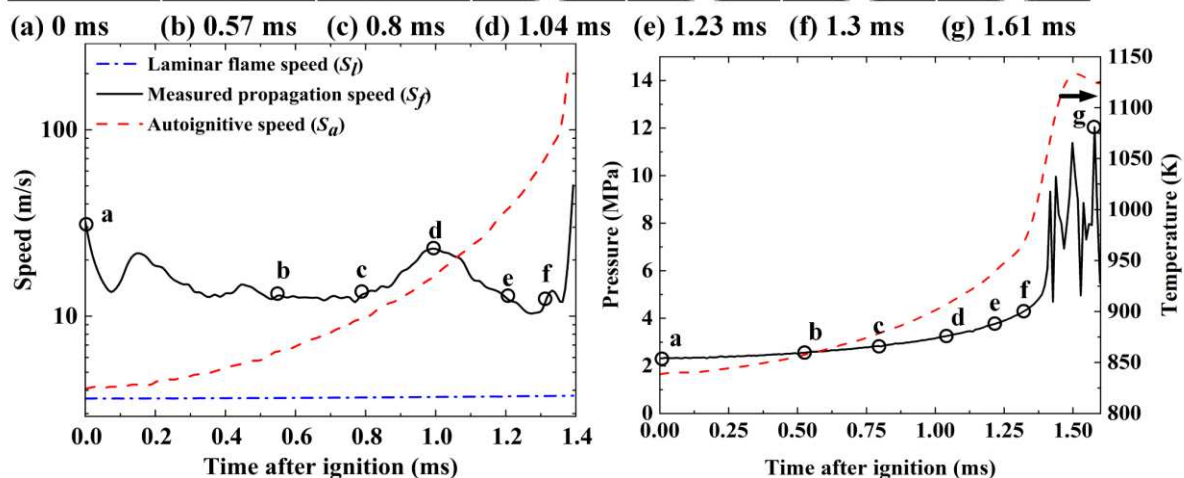
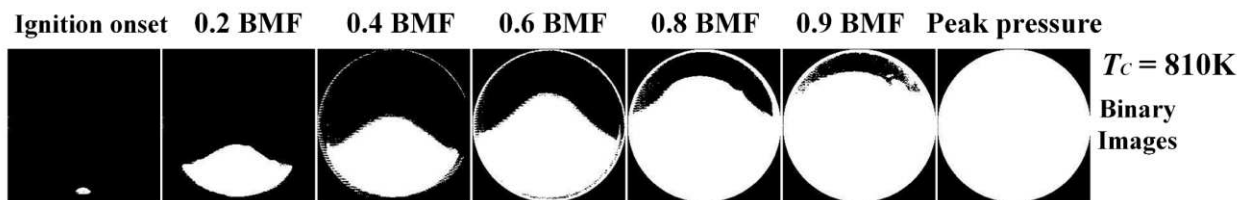


Fig. 20.  $T_c = 790$  K.

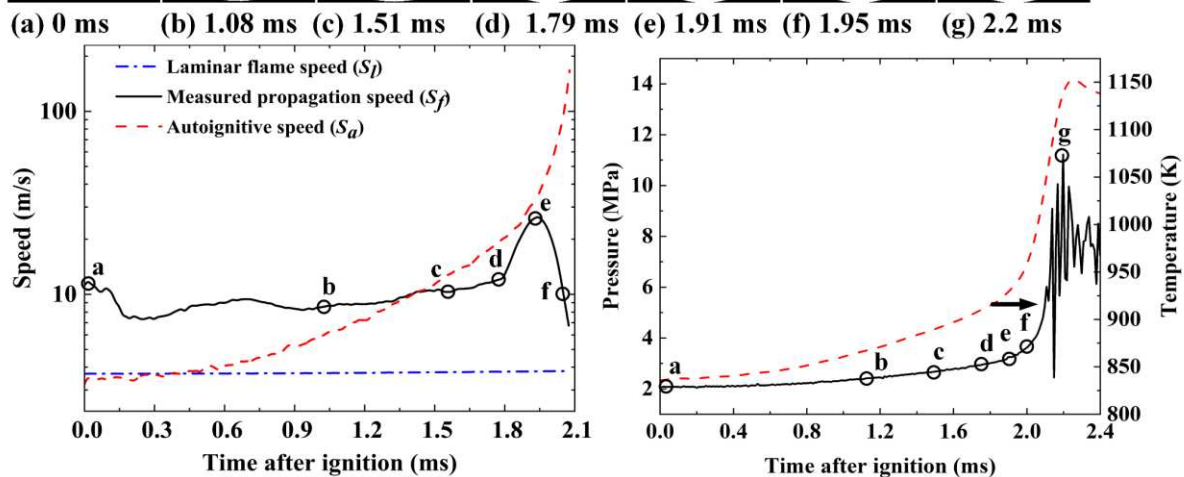
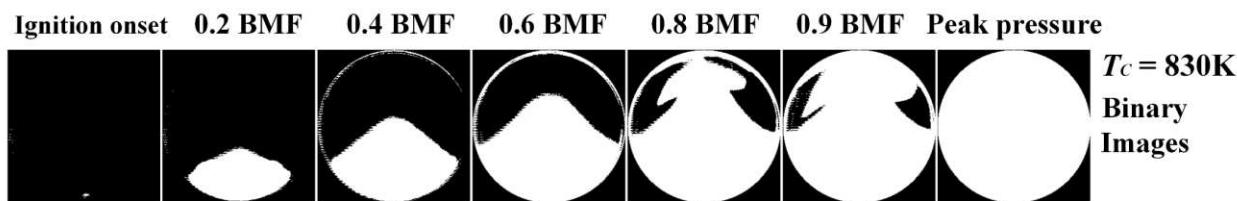
For  $T_c = 790$  K as shown in Fig. 20, one hot spot is observed initially, propagating from the bottom left of the cylinder. The image at (f) shows another, fairly extensive, new autoignition area above the propagation front. Initially, from point (a) to (b) the calculated autoignitive speed has the same trend as the measured speed. After point (f) this correspondence redeveloped, with an upturn in measured propagation speed, and with a pressure increase to 10 MPa, generating oscillations of 2.5 MPa amplitude. Still within the NTC regime, with high measured propagation speeds and pressure oscillations gaining strength, detonation is approaching. Transition to an ultimate detonation is beginning and is discussed in detail in Section 4.3.



(a) Speeds of Reactive Fronts      (b) Pressure and unburned gas temperature profiles

Fig. 21.  $T_c = 810\text{ K}$ .

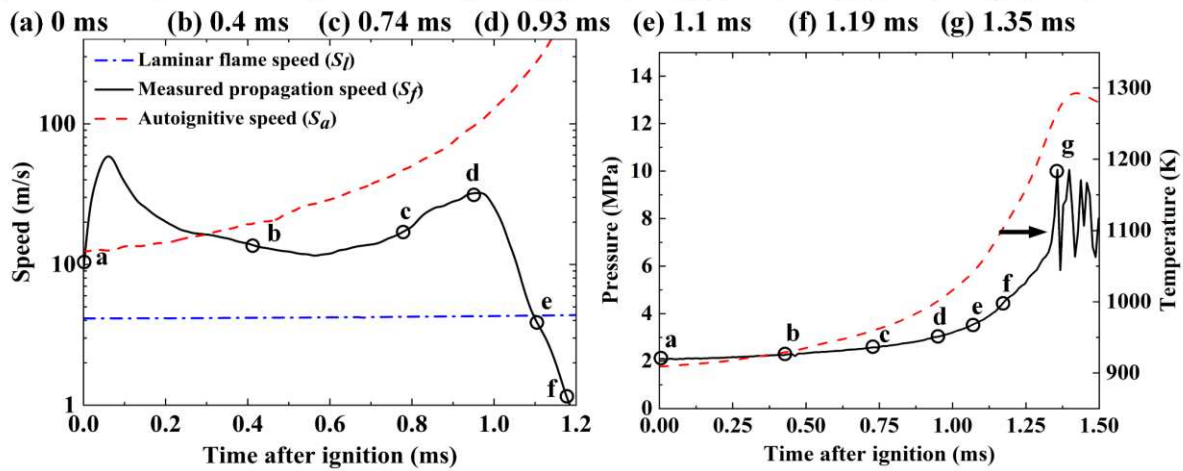
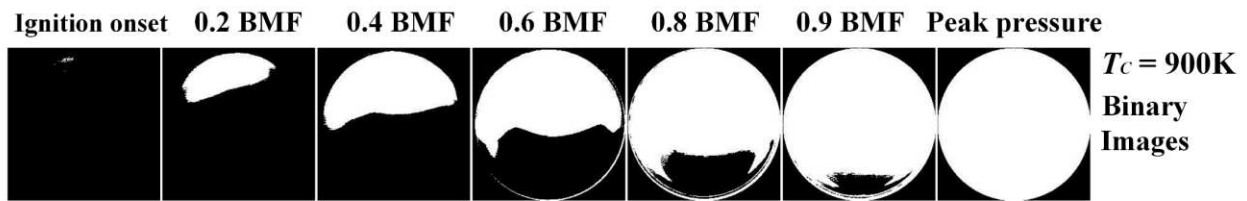
The binary images in Fig. 21 display a single initiating hot spot at  $T_c = 810\text{ K}$ , showing upwards propagation. Initially the computed autoignition speed approached the measured speed, but this is not sustained, although there is a final sharp increase in measured and computed speeds, and the final generation of strong pressure oscillations. This is close to the high temperature limit of the NTC regime of  $830\text{ K}$ .



(a) Speeds of Reactive Fronts      (b) Pressure and unburned gas temperature profiles

Fig. 22.  $T_c = 830$  K.

In Fig. 22, at  $T_c = 830$  K, the measured propagation speed exceeds the theoretical autoignitive values up to a temperature of about 880 K. There are some strong pressure oscillations leading ultimately to detonation. From points (c) to (d), the measured propagation and theoretical autoignitive speeds then become closer before a sharp reduction of the measured points, with increasing temperature. Reaction is becoming more concentrated in the final stages.



(a) Speeds of Reactive Fronts      (b) Pressure and unburned gas temperature profiles

Fig. 23.  $T_c = 900$  K.

The binary image (a) in Fig. 23 shows the ignition hot spot initiating at the top left of the cylinder. From the onset of ignition point (a) to point (d), the computed autoignitive speed follows the measured propagation speed tolerably well, until the later stages when it declines, pressure oscillations increase, and detonation begins to develop moderately close to the autoignitive speed. Thereafter, the measured propagation speed starts to fall quite sharply. The reason for this final decrease in propagation speed is probably associated with the reaction wave approaching the cylinder wall, and the development of pressure oscillations with an amplitude of 2.0 MPa. There is a high reaction rate, despite the lack of any appearance of a strongly coherent reaction front, probably associated with the development of a detonation.

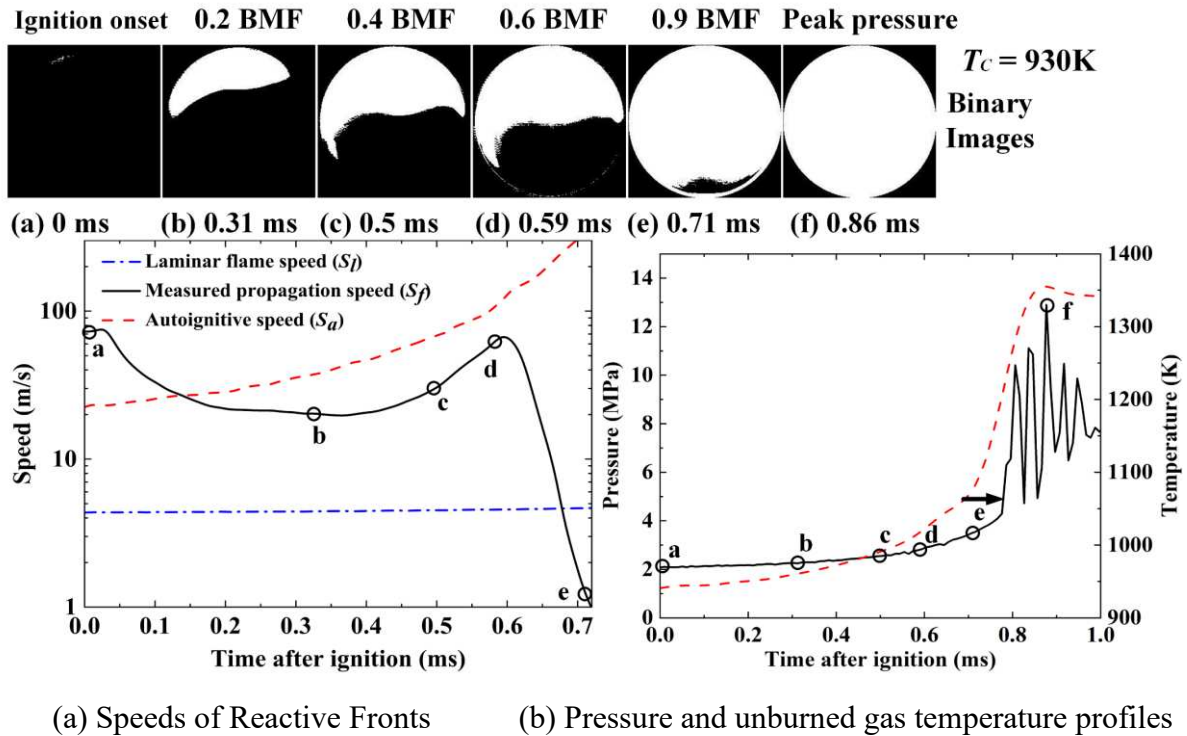


Fig. 24.  $T_c = 930$  K.

In Fig. 24, at the highest critical temperature of  $T_c = 930$  K, both the ignition and propagation direction are observed to be similar to those at  $T_c = 900$  K. There is good correspondence between the measured propagation and calculated autoignitive speeds, again until the final stage and wall interaction, when detonation is developing. The pressure oscillation is observed after point (e) with amplitude of 4.0 MPa.

#### 4.2 Summary of propagation speeds and modes

The experimental data in Fig. 25 summarises all the reaction propagation speeds that have been presented. These embrace the NTC regime, but not the transition to detonation. Five of all the ignitions started at the top of the cylinder and six at the bottom. The measured propagation speeds,  $S_m$ , the calculated autoignitive speed,  $S_a$ , and laminar flame speeds,  $S_l$ , are all just after compression to the different values of  $T_c$  and are shown in Fig. 25. The  $S_m$  values are defined as mean propagation speed from the onset of autoignition to the point where 5% burned mass fraction. Both  $S_a$  and  $S_l$  represent speeds at the corresponding  $T_c$  and pressure of 2.0 MPa.

At the outset, with  $T_c = 640$  K, the measured propagation speed was closest to the laminar flame and lower than the theoretical autoignitive speed. Then, moving to the higher  $T_c$  values of 670 K and 690 K, the measured propagation speeds became 9.3 m/s and 18.8 m/s respectively, about ten time higher

than the laminar flame speed, and slightly higher than the calculated autoignitive speed, but suggesting autoignitive propagation.

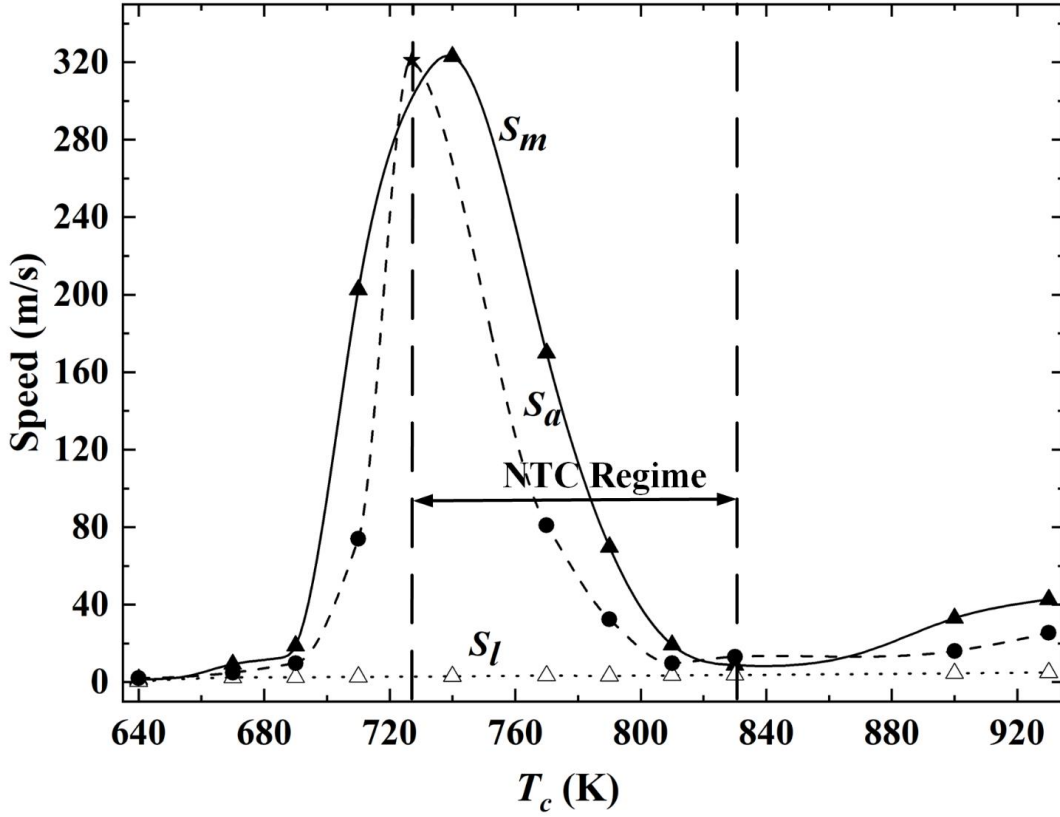


Fig. 25. Measured propagation speed, calculated autoignitive speed and laminar flame speed, plotted against  $T_c$ , for explosions, from 640 K to 930 K.

Close to the start of the NTC regime the measured propagation speed,  $S_m$ , sharply increases to 210 m/s, whilst the computed autoignitive speed,  $S_a$ , only increases to 72 m/s. Further into the NTC regime, at  $T_c = 740$  K, the measured propagation speed reaches a maximum value of 323 m/s. As discussed in Section 3.3, evaluation of autoignitive speeds is particularly challenging in the NTC regime, as also can be seen from the values of  $\frac{\partial \tau_i}{\partial T}$  in Fig. 7. In the analysis shown in Fig. 26, a finer temperature interval of 0.1 K was employed to examine the effects on  $\tau_i$ ,  $\frac{d\tau_i}{dT}$  and  $u_a$  at a constant pressure of 2 MPa. The transition into the NTC regime is observed at 727.4 K, where  $\frac{d\tau_i}{dT}$  falls below -0.0001 (ms/K). This change correlates with an  $u_a$  as high as 7000 m/s. Theoretically, further refining of the temperature interval leads to  $\frac{d\tau_i}{dT}$  nearing zero, implying an infinitely high  $u_a$ . On the basis of this figure, a gradient of 0.0037 ms/K at 727.2 K was chosen from the derived values of  $\frac{\partial \tau_i}{\partial T}$  in Fig. 26.

This low value yielded one of  $S_a = 315$  m/s, shown plotted on Fig. 25 by the asterisk.

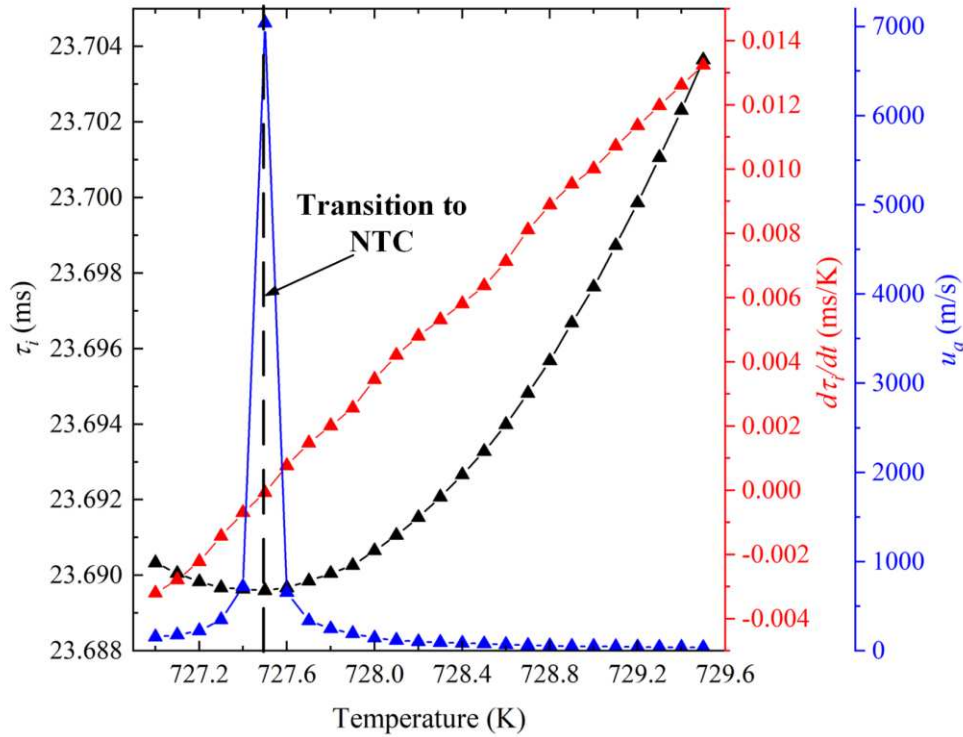


Fig. 26. Variation of  $\tau_i$ , its derivative  $\frac{d\tau_i}{dT}$  and autoignitive velocity  $u_a$ , across the NTC regime.

Uncertainties about the temperature gradient in the NTC regime, give rise a to a high variability in the values of calculated autoignitive speed. However, at the upper NTC limit of 830 K, just after leaving the NTC regime, all three speeds are close to 8 m/s. Thereafter, both measured and computed autoignitive speeds increase sharply in the high temperature regime, enhancing transitions to detonation.

#### 4.3 Processing the Onset of Detonation

The final stages in the data processing involve the early development of detonations and the associated increases in pressure and temperature. Transition to detonation entails a more active role for the  $\zeta$  and  $\varepsilon$  parameters, both inside and outside the Detonation Peninsula. Figures 27 and 28 show how, with increasing rapidity, values of  $\zeta$  fall, whilst those of  $\varepsilon$  increase, heralding the approaching detonation. Calculation of  $\zeta$  and  $\varepsilon$  is described in Section 3.4. Here, these values are found for the measured parameters and shown alongside them. Simultaneously, amplitudes of the pressure oscillations increase as the reaction front approaches the chamber wall.

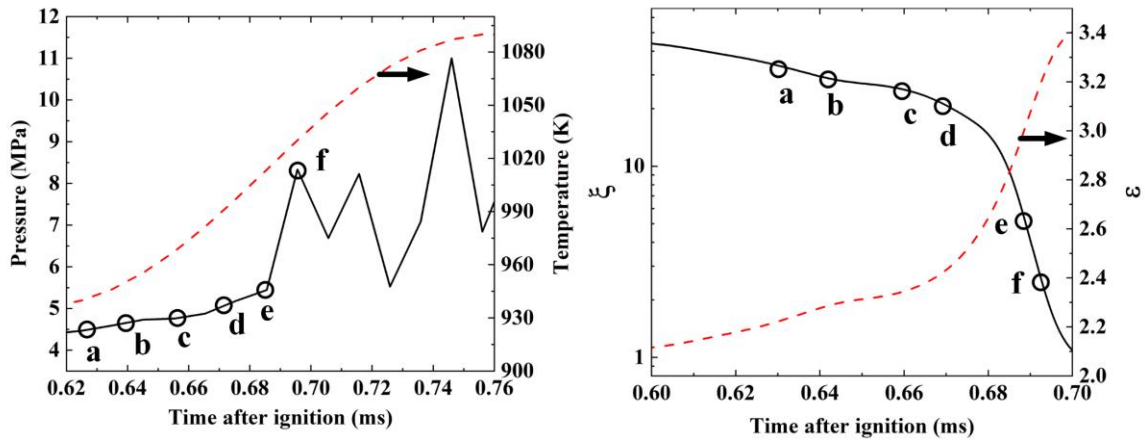
Although the monochrome images in the two figures display poor optical contrast, they nevertheless

present a more direct visualisation of the extending high-pressure front in both figures. After starting at points (d) and (e), there is a strong build-up of pressure at the wall.

$T_c = 790 \text{ K}$



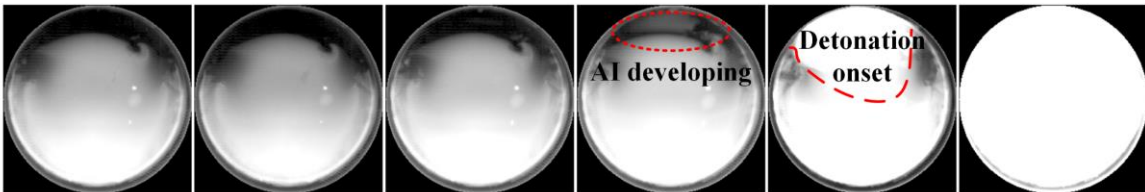
(a) 0.627 ms (b) 0.64 ms (c) 0.657 ms (d) 0.672 ms (e) 0.687 ms (f) 0.695 ms



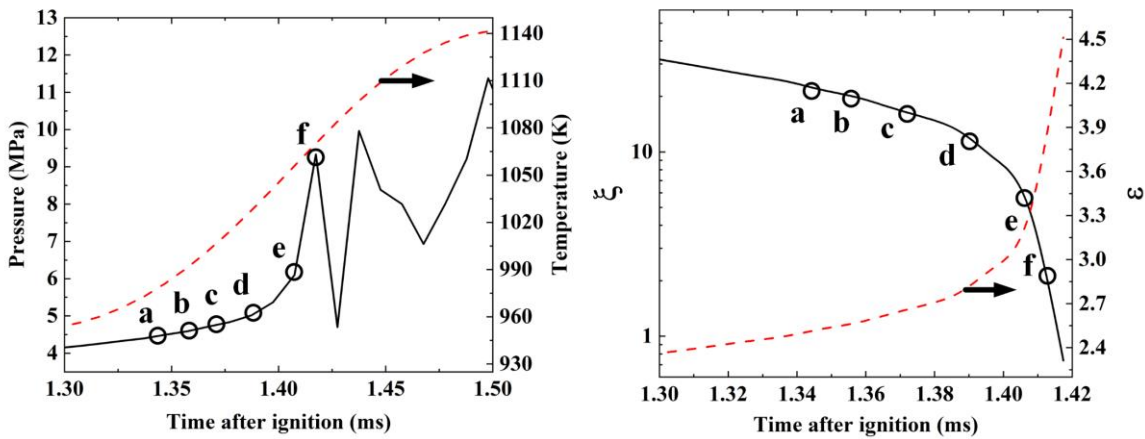
(a) Pressure and mixture temperature profiles (b)  $\zeta$  and  $\epsilon$  profiles

Fig. 27.  $T_c = 790 \text{ K}$ , High Speed Detonation Images, derivations of  $\zeta$  and  $\epsilon$ .

$T_c = 810 \text{ K}$



(a) 1.343 ms (b) 1.358 ms (c) 1.373 ms (d) 1.388 ms (e) 1.407 ms (f) 1.418 ms



(a) Pressure and mixture temperature profiles (b)  $\zeta$  and  $\epsilon$  profiles

Fig. 28.  $T_c = 810$  K, High Speed Detonation Images, derivations of  $\zeta$  and  $\varepsilon$ .

Earlier study focusing on the  $\zeta$  and  $\varepsilon$  appear in [3] and [20]. Entering the Detonation Peninsula indicates a potential transition to detonation. Outside the Peninsula any propagations are likely to be subsonic autoignition or flame propagation. It is possible to assess the relative severities of the different autoignitions. The different mixtures are characterised in Table 1 in terms of  $T_c$  values. On all Peninsulas triangle symbols indicate the absence of significant pressure oscillations. The area of a circular symbol is proportional to the amplitude of the pressure oscillations, and the number on the right indicates the mean oscillating pressure in MPa. Explosion characteristics for different values of  $T_c$  for Three pairs of explosions are analysed.

#### 4.4 Peninsulas for $T_c = 790$ K and $810$ K

As can be seen in Fig. 29, both of the explosions  $T_c$  culminated in moderate detonations. These are the ultimate characteristics for the experiments described in detail in Figs. 27 and 28 and the interpretations of them in Section 4.3. Detonations eventually developed. Prior to this there were subsonic autoignitions. A detonation with  $T_c = 790$  K, with  $\varepsilon = 3.5$  and  $\zeta = 2.4$  yields the lowest Detonation Parameter,  $\beta=(\varepsilon/\zeta)$  of 1.5.

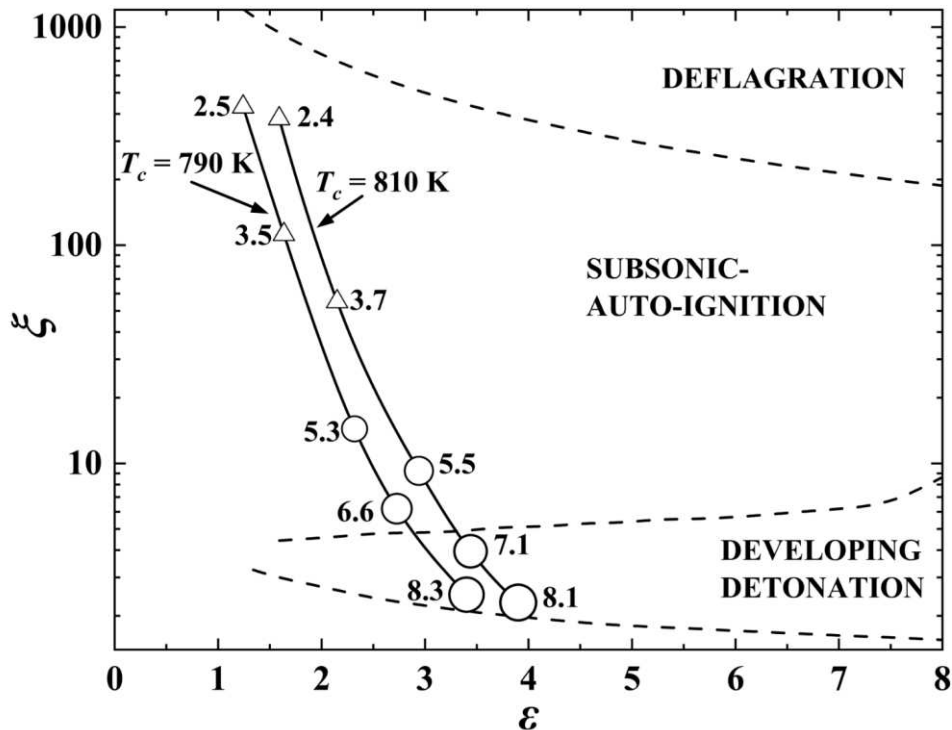


Fig. 29. Peninsulas  $\zeta$  -  $\varepsilon$  diagram for  $T_c = 790$  K and  $810$  K.

#### 4.5 Peninsulas for $T_c = 710$ K and $770$ K

Figure. 30 shows the striking aspect of these results is that no detonations developed, and there are few instances of strong autoignitions. These are low reactivity results. The experimental data are in Figs. 17 and 19. At no stage do the derived values enter the peninsula. There are no detonations, just subsonic autoignitions.

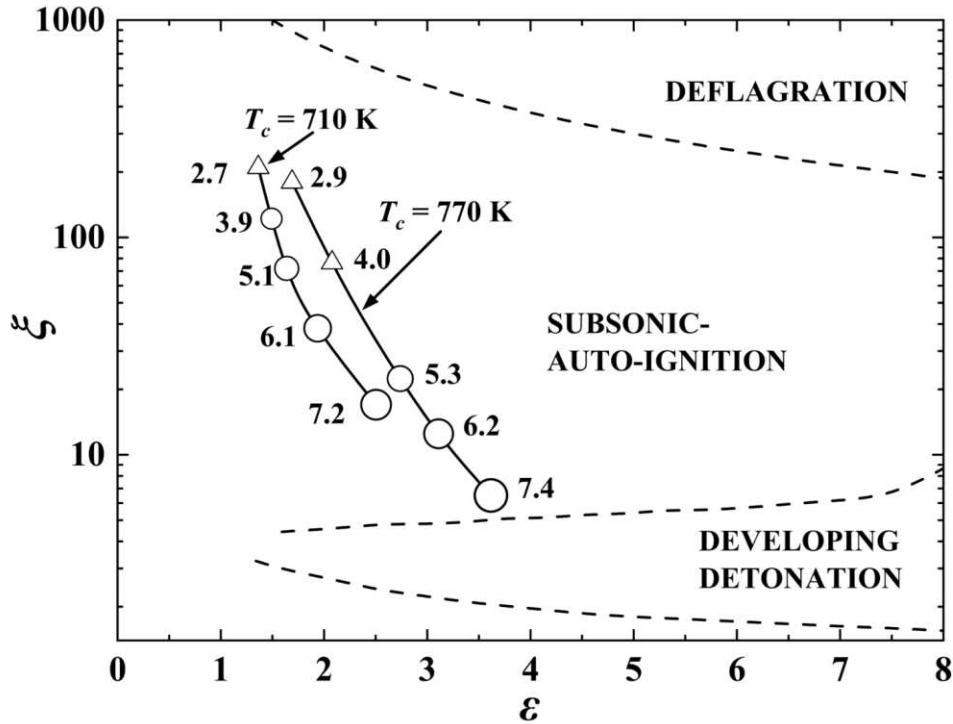


Fig. 30. Peninsulas  $\zeta - \epsilon$  diagram for  $T_c = 710$  K and 770 K.

#### 4.6 Peninsulas for $T_c = 830$ K and 930 K

Both explosions culminate fairly soon in detonations and are similarly reactive. Fig. 31 shows a noteworthy rapid increase in  $\epsilon$  to 5.1, at a low value of  $\zeta$  of around 1.8. High energy is being fed at a high rate into a developing acoustic wave. If the rate is high enough it can be classified as super-knock. In [4] super-knock is attributed to a rather more severe detonation, with a value of  $\epsilon$  as high as 11, and a value of  $\zeta$  as low as 2.7. A high value of  $\epsilon$  can be nullified by a high value of  $\zeta$ . It is of interest to contrast these data with those at the lowest  $T_c$  value of 640 K, for which, all values of  $\epsilon$  were less than unity and all values of  $\zeta$  were more than 30. There were no pressure oscillations, no detonations, and it was possible to support laminar flame propagation.

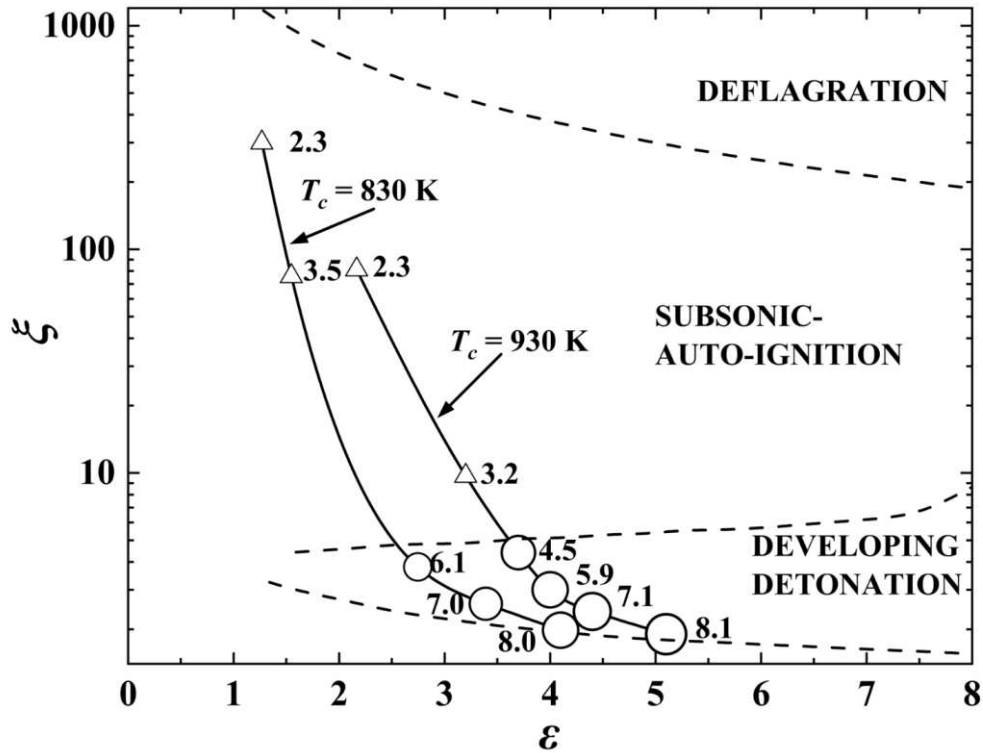


Fig. 31. Peninsulas  $\zeta - \varepsilon$  diagram for  $T_c = 830$  K and  $930$  K.

## 5. Pressure Perturbations

The amplitude of the pressure fluctuations increases as the reaction progresses towards detonation and it is fruitful to plot the normalised amplitudes of the pressure oscillations,  $\Delta P/P$ , against a Detonation Parameter,  $\beta$ , defined by,  $(\varepsilon/\zeta)$  as in Fig. 32. This formulation results in  $\beta = \frac{u_a r_0}{\tau_e a^2}$  and a large value of  $\beta$  suggests a scenario of rapid and extensive reaction, possibly leading to detonation. Figure 32 shows such a variation of  $\Delta P/P$  with  $\beta$ , an indicator of the progression through the different phases of the reaction, which are indicated. No significant pressure amplitudes are detected in the initial low temperature regime with brief laminar flames and here  $\beta$  was estimated to be less than 0.002. As  $T_c$  increased, autoignitive velocities increased and, with that, so also did the amplitudes of the pressure fluctuations.

With  $T_c = 710$  K, a temperature slightly lower than that for entry to the NTC regime, increasingly rapid autoignitive speeds increased the amplitudes of the pressure oscillations significantly. After the exceptionally high autoignitive velocity shown, within the NTC regime in Fig. 25, at 740K, the higher pressures developed close to the chamber walls, leading ultimately to detonation, this is shown in its most complete in Fig. 31, and as knock and super-knock in Fig. 32. Super-knock occurred with  $\beta =$

6.8 and with  $\Delta P/P = 0.42$ .

The appropriateness of the correlation in Fig. 32 is understandable. A high value of the Detonation Parameter is associated with a low value of  $\tau_e$ , and an associated high value of  $\varepsilon$ , together with an associated high value of  $u_a$  and low value of  $\zeta$ .

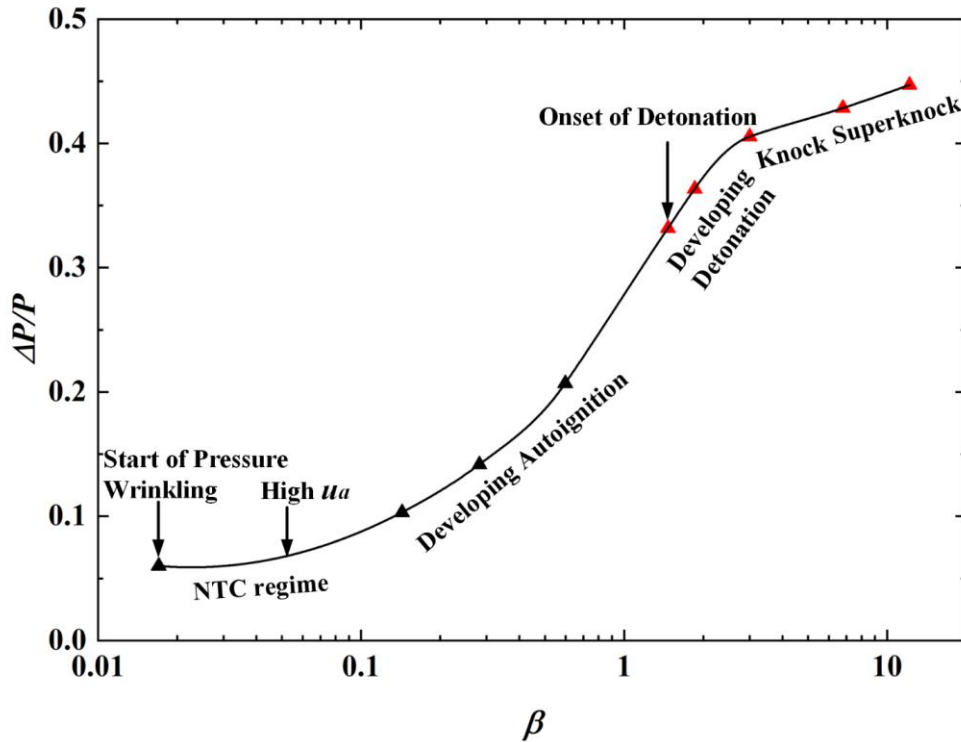


Fig. 32.  $\Delta P/P$  as a function of Detonation Parameter  $\beta$ .

## 6. Conclusions

- i. Pressures, temperatures, reaction propagation speeds, and transitions to detonation have been measured, or inferred, after rapid compression to 2.0 MPa, of a stoichiometric mixture of *i*-octane/oxygen, with variable proportions of inert gases.
- ii. At the lowest compression temperature,  $T_c$ , of 640 K, a significant reaction propagation speed was that of a slightly wrinkled laminar flame. At the higher values of  $T_c$ , autoignitive propagation developed, with diminishing evidence in the later stages of any minor laminar burning.
- iii. Up to  $T_c = 710$  K there was tolerable agreement between the measured propagation speed and the computed autoignitive speed. At this temperature, at the threshold of the NTC regime, pressure oscillations of increasing amplitude, but not detonative, began to develop.
- iv. Inside the NTC regime and at  $T_c = 740$  K, the measured propagation speed attained a high peak

value of 323 m/s. This might be explained by the vagaries of this speed being inversely proportional to  $\frac{\partial \tau_i}{\partial T}$ , particularly as these derivative approaches zero near the transition to the NTC regime.

v. Although in the NTC regime, the value of  $\frac{\partial \tau_i}{\partial T}$  can increase autoignitive speeds, it does not directly induce detonation.

vi. The transition to detonation was traced through the changes in  $\zeta$ , the chemical kinetically derived  $\varepsilon$ , and the Detonation Peninsulas.

vii. Detonation occurred in five of the eleven explosions listed in Table 1. Entry to the Detonation Peninsula occurred at  $T_c = 790$  K and a mild detonation ensued, with  $\zeta = 2.4$  and  $\varepsilon = 3.5$ .

viii. At  $T_c = 710$  K, pressure oscillations of increasing amplitude were generated by the increasingly rapid autoignitive speeds. The normalised amplitude of the pressure oscillations,  $\Delta P/P$ , increased with a proposed Detonation Parameter, defined by  $\beta$ , a value of  $\beta = 1.5$  and  $\Delta P/P = 0.33$  as an indicator of progression towards detonation.

ix. After the initial low autoignitive velocities their steady increase leads progressively to increases pressure oscillation amplitudes build up at the chamber walls, developing detonation, detonation, and finally super-knock, with  $\varepsilon = 11$ ,  $\zeta = 2.7$  and  $\beta = 4.1$  [4].

x. The study shows the chemical transformations occurring in a RCM to be chemically complex and different from the ideal cycle. Nevertheless, overall measured ignition delay times are practically valuable for the avoidance of both knock in internal combustion engines and the occurrence of hazardous explosions [16].

## References

- [1] C. Sung, H. Curran, Using rapid compression machines for chemical kinetics studies, *Prog. Energy Combust* 44 (2014) 1-18.
- [2] D. Bradley, M. Lawes, M. Materego, Interpretation of auto-ignition delay times measured in different rapid compression machines, In 25th International Colloquium on the Dynamics of Explosions and Reactive systems (2015), Leeds.
- [3] L. Bates, D. Bradley, G. Paczko, N. Peters, Engine hot spots: Modes of auto-ignition and reaction propagation, *Combust. Flame* 166 (2016) 80-85.
- [4] G. Kalghatgi, D. Bradley, J. Andrae, A. Harrison, The nature of “superknock” and its origins in SI engines, In IMechE conference on internal combustion engines: performance fuel economy and emissions (2009) 8-9.
- [5] W. Liu, Y. Qi, R. Zhang, Z. Wang, Flame propagation and auto-ignition behavior of iso-octane across the negative temperature coefficient (NTC) region on a rapid compression machine, *Combust. Flame* 235 (2022) 111688.
- [6] I. Gorbatenko, D. Bradley, A. Tomlin, Auto-ignition and detonation of n-butanol and toluene reference fuel blends (TRF), *Combust. Flame* 229 (2021) 111378.
- [7] A. Robert, S. Richard, O. Colin, T. Poinso, LES study of deflagration to detonation mechanisms in a downsized spark ignition engine, *Combust. Flame* 162 (2015) 2788-2807.
- [8] W. Affleck, A. Thomas, An opposed piston rapid compression machine for pre-flame reaction studies, *Proc. Inst. Mech. Eng* 183 (1968) 365-387.
- [9] J. Pan, Z. Hu, H. Wei, M. Pan, X. Liang, G. Shu, L. Zhou, Understanding strong knocking mechanism through high-strength optical rapid compression machines, *Combust. Flame* 202 (2019) 1-15.
- [10] Y. Wang, Y. Qi, W. Liu, Z. Wang, Investigation of methanol ignition phenomena using a rapid compression machine, *Combust. Flame* 211 (2020) 147-157.
- [11] N. Otsu, A threshold selection method from gray-level histograms, *IEEE transactions on systems, man, and cybernetics* 9 (1979) 62-66.
- [12] C. Morley, GASEQ: a chemical equilibrium program for Windows, <http://www.gaseq.co.uk>,

(2005).

[13] CHEMKIN-Pro 19.2, Reaction Design, San Diego, California, 2017.

[14] M. Mehl, W. Pitz, C. Westbrook, H. Curran, Kinetic modeling of gasoline surrogate components and mixtures under engine conditions, *Proc. Combust. Inst.* 33 (2011) 193-200.

[15] D. Bradley, R. Hicks, M. Lawes, C. Sheppard, R. Woolley, The measurement of laminar burning velocities and Markstein numbers for iso-octane–air and iso-octane–n-heptane–air mixtures at elevated temperatures and pressures in an explosion bomb, *Combust. Flame* 115 (1998) 126-144.

[16] S. Goldsborough, S. Hochgreb, G. Vanhove, M. Wooldridge, H. Curran, C. Sung, Compression machine studies of low- and intermediate-temperature autoignition phenomena, *Prog. Energy Combust. Sci.* 63 (2017) 1-78.

[17] P. Dai, Z. Chen, S. Chen, S. Y. Ju, Numerical experiments on reaction front propagation in n-heptane/air mixture with temperature gradient, *Proc. Combust. Inst* 35 (2015) 3045-3052.

[18] G.T. Kalghatgi, D. Bradley, Pre-ignition and ‘super-knock’ in turbo-charged spark-ignition engines. *Int. J. Engine Res* 13(2012) 399-414.

[19] A.E. Lutz, R.J. Kee, J.A. Miller, H.A. Dwyer, A.K. Oppenheim, Dynamic effects of autoignition centers for hydrogen and C1, 2-hydrocarbon fuels, *Symp. (Int.) Combust.* 22 (1988) 1683-1693.

[20] X. Gu, D. Emerson, D. Bradley, Modes of reaction front propagation from hot spots, *Combust. Flame* 133 (2003) 63-74.